University of Cincinnati

Date: 7/18/2013

I, Daniel M Santel , hereby submit this original work as part of the requirements for the degree of Doctor of Philosophy in Physics.

It is entitled:

Measurement of the Cross-section s(e+e->Y(nS)pi+pi-) vs. sqrt(s) in the Region of 10.6 GeV to 11.02 GeV

Student's name: **Daniel M Santel**

This work and its defense approved by:

Committee chair: **Kay Kinoshita, Ph.D.**

Committee member: **Carlos Bolech, Ph.D.**

Committee member: **Alexander Kagan, Ph.D.**

Committee member: **Brian Meadows, Ph.D.**

UNIVERSITY OF
Cincinnati

5638

Measurement of the cross-section $\sigma(e^+e^- \to \Upsilon(nS)\pi^+\pi^-)$ vs. $\sqrt{s}$ from 10.6–11.02 GeV

A dissertation submitted to

the Graduate School

of the University of Cincinnati

in partial fulfilment

of the requirements for the degree of

Doctor of Philosophy

in the Department of Physics

of the College of Arts and Sciences

by

Daniel Santel

B.S. University of Cincinnati

June 2006

Committee Chair: Kay Kinoshita, Ph.D

Abstract

We report a new measurement of the cross-section $\sigma(e^+e^- \to \Upsilon(nS)\pi^+\pi^-)$ (n = 1,2,3) in the region $\sqrt{s} = 10.63$ GeV/c^2 to 11.02 GeV/c^2, including sixteen 1 fb^{-1} scan points not previously reported on, six previously reported scan points, and 121 fb^{-1} at the $\Upsilon(5S)$ resonance, all taken with the Belle detector at KEK in Tsukuba, Japan. The shape is compared with that of $\sigma_b = \sigma(e^+e^- \to b\bar{b} \to hadrons)$, measured using the sixteen 1 fb^{-1} scan points and sixty-one 50 pb^{-1} scan points. This analysis supersedes the previous measurement with additional scan and $\Upsilon(5S)$ data, by fitting both cross-sections using the same model, and by introducing a model-insensitive correction for the $\Upsilon(nS)\pi^+\pi^-$ acceptance. We measure the mass and width of the $\Upsilon(5S)$, $M_{5S} = 10884.4 \pm 1.4 \pm 1.6$ MeV and $\Gamma_{5S} = 50 \pm 5 \pm 3$ MeV, consistent with the measurements obtained from a concurrent R_b analysis.

I

Acknowledgments

This work would not have been possible without the help and support of too many teachers, colleagues, friends, and family to list in full.

I thank my advisor Kay Kinoshita for her patience when I was slow to comprehend, focus when I was sidetracked by tangents, and guidance when I did not know how to proceed. I would like to every member of the Belle Collaboration and the KEKB accelerator team whose hard work make analyses like this possible. Thanks go to all of the other members of UC's Belle group, who provided useful suggestions, asked hard questions, and variously helped me in Japan, with ROOT, and with Belle's software. I thank the faculty of the UC physics department and all of my teachers over the years for encouraging me in all of my academic pursuits.

I thank my sisters and friends for all of their support over the years, within physics and without. Tammy, Kristen, Zach, Marlena, Joe, Katy, and many others: thank you.

Special thanks go to my parents, who instilled in me a love of education and science, who insisted I go to college, and who supported me when I decided to stay there for more than a decade.

Contents

List of Tables

VIII

List of Figures

Chapter 1

History and Motivation

In 2006, with 23 fb^{-1} taken at 10.867 GeV, the Belle collaboration measured the production rates of $e^+e^- \rightarrow \Upsilon(5S) \rightarrow \Upsilon(nS)\pi^+\pi^-$ (n = 1, 2, 3) ($\Upsilon(5S)$ is also known as $\Upsilon(10860)$) to be two orders of magnitude larger than expected, based on the rates of the transitions $\Upsilon(mS) \rightarrow \Upsilon(1S)\pi^+\pi^-$ (m = 2, 3, 4) [11].

This anomalous result led to a scan in 2007 [10] at center-of-mass (CM) energies around the $\Upsilon(5S)$ resonance to measure both the $\Upsilon(nS)\pi^+\pi^-$ cross-section and the hadronic cross-section, R_b, where R_b is defined as $\sigma(b\bar{b})/\sigma(\mu\mu)$. The $\sigma(\Upsilon\pi\pi)/\sigma(\mu\mu)$ distribution was obtained from a fit of a single Breit-Wigner (BW) function (associated with the $\Upsilon(5S)$) with a coherent constant term, while the R_b analysis used a fit of two coherent BW functions (associated with the $\Upsilon(5S)$ and $\Upsilon(6S)$), a coherent constant term, and an incoherent constant term. The mass and width of the $\Upsilon(5S)$-associated BW in each fit were compared, and the differences were $M_{\Upsilon\pi\pi} - M_{R_b} = 9 \pm 4$ MeV and $\Gamma_{\Upsilon\pi\pi} - \Gamma_{R_b} = -15^{+11}_{-12}$ MeV. With systematic uncertainties, the deviation of the $\sigma(\Upsilon\pi\pi)$ fit compared to a fit using the shape parameters from the R_b was 2.0σ.

The BaBar experiment also measured R_b in 2008 in the region of $\sqrt{s} = 10.54 - 11.20$ GeV and reported masses, widths, and phases relative to continuum for $\Upsilon(10860)$ and $\Upsilon(11020)$ [7]. A summary of the previous results from Belle and Babar are shown in Table 1.1.

A follow-up scan in 2010 at Belle was designed to yield higher precision in $\sigma(e^+e^- \rightarrow$

$\Upsilon(nS)\pi^+\pi^-$) and R_b, and to investigate the hypotheses involving possible Y_b-type resonances (akin to the $Y(4260)$ seen in similar decays in the charm sector) in the $\Upsilon(5S)$ region [5].

Related analyses and results included the observation of two new charged bottomonium-like resonances in $\Upsilon(10860) \to h_b(n)\pi\pi$ and $\Upsilon(10860) \to \Upsilon(nS)\pi\pi$ decays, with 121.4 fb^{-1} of on-resonance data [8].

Table 1.1: Results from R_b (Belle and Babar) and $\sigma(\Upsilon\pi\pi)$ (Belle) measurements.

Analysis	M_{10860} (MeV)	Γ_{10860} (MeV)	M_{11020} (MeV)	Γ_{11020} (MeV)
Belle 2007 $\sigma(\Upsilon\pi^+\pi^-)$	$10888.4^{+2.7}_{-2.6}$	$30.7^{+8.3}_{-7.0}$	N/A	N/A
Belle 2007 R_b	10879 ± 3	46^{+9}_{-7}	10996 (fixed)	37 (fixed)
Babar 2010 R_b	10876 ± 2	43 ± 4	10996 ± 2	37 ± 3

Figure 1.1: Belle's previous $\sigma(\Upsilon\pi\pi)$ and R_b cross-section measurements [10].
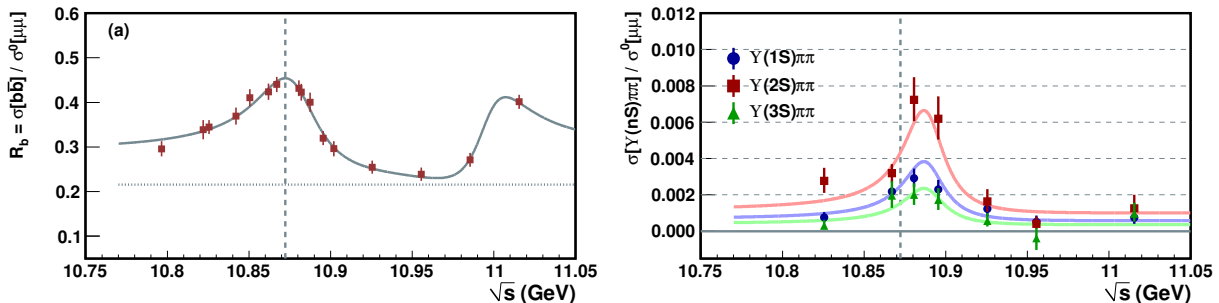
Chapter 2

Introduction

2.1 Standard Model

The Standard Model (SM) is a theoretical framework devised to describe the elementary particles and their interactions via the fundamental forces, including the weak, strong, and electromagnetic forces, and excepting, for now, gravity. The SM includes the six quarks known as the *up* (u), *down* (d), *charm* (c), *strange* (s), *top* (t), *bottom* (b), the six leptons (e, ν_e, μ, ν_μ, τ, ν_τ) and the gauge bosons that mediate the weak force ($W^\pm$, Z_0), strong force (gluons g) and electromagnetic force (photons γ). The quarks and leptons are each divided into three generations of doublets. The SM also includes the Higgs boson (H^0), an elementary scalar boson associated with the Higgs field. A particle consistent with being an H^0 was first observed in 2012 by CMS [2] and ATLAS [3]. A summary of the standard model particles is shown in Figure 2.1.

2.1.1 Electromagnetic interactions

The electromagnetic interaction is described by the formalism of quantum electrodynamics (QED). The interaction is mediated by massless γs coupling to electric charge. Feynman diagrams and the associated rules are a fairly straightforward method frequently used to calculate QED interactions to the first couple of orders. The QED formalism, and the
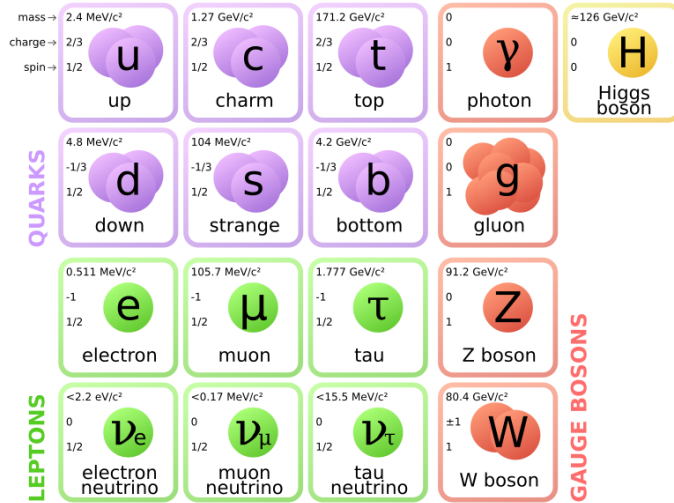
Figure 2.1: The particles in the Standard Model, and their masses, charges, and spins. The masses of the quarks, in particular the light quarks, are estimates and do not necessarily represent the quark mass in a hadron. Image credit [21].

drawing and use of Feynman diagrams, are covered in some detail in many elementary particle physics textbooks [15] [24].

2.1.2 Weak interactions

The weak interaction is mediated by the massive $W^\pm$ and Z_0 ($m_W = 80.4$ GeV, $m_Z = 91.2$ GeV) bosons, which couple to all leptons and quarks. The weak force differs from the others described in the SM in that it is the only one that can change the flavor of quarks, and is also the only verified source of CP violation. The $W^\pm$ and Z_0 acquire their masses via the Higgs mechanism (p. 692 of Reference [24]), and it is due to the mass of the mediators that the weak interaction is very short range ($\approx 10^{-18}$ m). This also causes the weak interaction to be comparatively "slower" and causes particles that decay predominantly via the weak interaction to be longer-lived (such as the neutron, with a lifetime on the order of 15 minutes). Many elementary particle physics textbooks cover the weak interactions in more detail [15] [24].

2.1.3 Strong interactions

The theory describing the strong interaction is quantum chromodynamics (QCD), which includes the interactions of color-charged objects. The color-charge is limited to quarks and gluons, the latter being the mediators of the strong force. Asymptotic freedom is a property of QCD, which means that the interactions between quarks and gluons becomes asymptotically weaker as energy increases and distance decreases. Conversely, QCD predicts that the strong force *increases* with the distance between coupled objects, and the energy required to produce "free" quarks is inevitably enough to create *more* quarks, leading to hadronization into mesons and baryons. This in part explains why isolated gluons and quarks are never seen.

The theory requires then that any finite-energy combination of quarks and gluons must be color-neutral. Unlike the electromagnetic charge, there are three each of color and anti-color charges (r, g, b, $\bar{r}$, $\bar{g}$, $\bar{b}$). The combination of a color and its anti-color is neutral, and the combination of the three colors (anti-colors) together is neutral. Thus, the simplest color-neutral states are mesons, combinations of a quark and an antiquark (with a color and its anti-color), and baryons (three quarks with the three colors) and anti-baryons (three anti-quarks with the three anti-colors). Other states would seem to be possible as well, but have not been conclusively observed, including glueballs (gg, ggg), hybrid mesons ($q\bar{q}g$), tetraquarks ($qq\bar{q}\bar{q}$), and pentaquarks ($qqq\bar{q}q$).

2.2 Spectroscopy of Quarkonia

Quarkonia are a special class of meson which are composed of one heavy quark and its own anti-quark. These states can be considered as analogous to similar particle/anti-particle bound states such as positronium. Quarkonia have similar spectra of excited states, with excitations in the principal quantum number (n), intrinsic angular momentum (spin, s), and orbital angular momentum ℓ. The term quarkonium is generally reserved for charm/anti-charm and bottom/anti-bottom pairings, as the up, down and strange quarks are too light to

draw the proper analogy, and top quarks are so massive that they decay by weak interactions before bound states can form.

The $s = 0$, $\ell = 1$ states are particularly relevant at e^+e^- accelerators, as they can be produced directly from processes involving annihilation to a virtual photon ($e^+e^- \to \gamma^* \to q\bar{q}$). For charmonium, these are the J/ψ and other $\psi(nS)$ states. For bottomonium, these are the $\Upsilon(nS)$.

Many of the expected states in the $c\bar{c}$ and $b\bar{b}$ spectra have been identified and measured to date. Figures 2.2 and 2.3 show many of the observed members of the charmonium and bottomonium families, respectively.
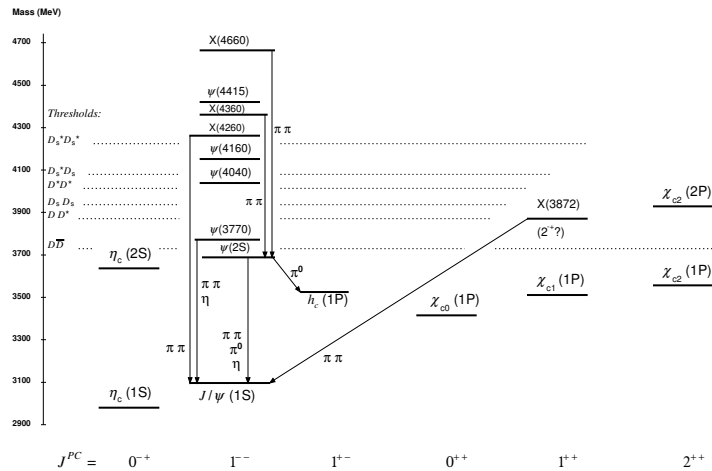
Figure 2.2: The charmonium family. [23].

2.3 Xs, Ys, Zs

There have also been a number of states discovered that do not fit into the naively expected spectroscopy of quarkonia. Just some of these are these are the $Y(4260)$ seen in $e^+e^- \to \gamma_{isr}J/\psi\pi^+\pi^-$ [6], the $Z^\pm(4430)$ in $B \to Z(4430)K \to \psi(2S)K\pi$ [13], two charged Zs in $B \to ZK \to \chi_{c1}\pi K$ [1], and the two charged Z_bs in $\Upsilon(5S) \to Z_b\pi \to \Upsilon(nS)\pi\pi$ [8]. There have been many interpretations of these particles, including four-quark states (such as tetraquarks
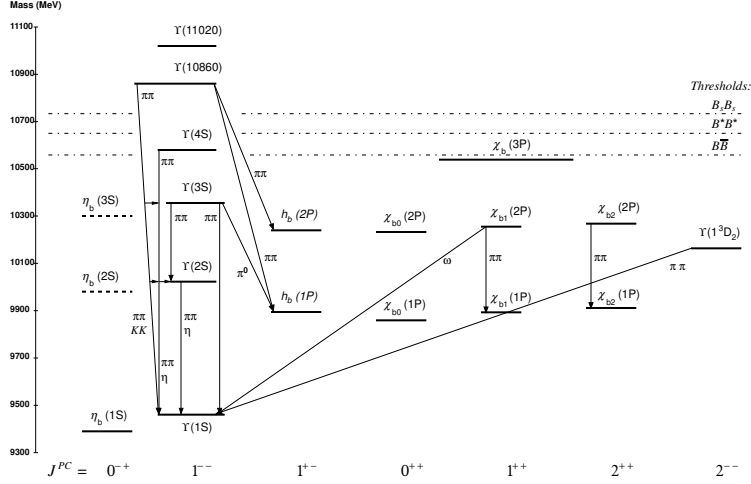
Figure 2.3: The bottomonium family. Image credit [23].

and mesonic molecules) and hybrid mesons (consisting of both a quark/anti-quark pair and at least one extra gluon).

2.4 Kinematics of Three Body Decays and Dalitz Plots

A Dalitz plot analysis is a common way to analyze three-body decays, as in many cases the three-body decay can be described by just two (of three possible) kinematic parameters, and displayed on a 2-dimensional plot. Let us consider a decay of a mother particle of mass and momentum M and P, respectively, with daughters of masses and momenta m_i, p_i (i = 1, 2, 3). We define $p_{ij} = p_i + p_j$, $m_{ij}^2 = p_{ij}^2$. The relationship then holds that

$$m_{12}^2 + m_{23}^2 + m_{13}^2 = M^2 + m_1^2 + m_2^2 + m_3^2, \tag{2.1}$$

and, for example, $m_{12}^2 = (P - p_3)^2 = M^2 + m_3^2 - 2ME_3$, where E_3 is the energy of daughter 3 in the rest frame of the mother.

The partial decay rate of a particle of mass M into n bodies, in the CM frame, is given (Kinematics Review in Reference [23]) in terms of the scattering amplitude $\mathcal{M}$ by

$$d\Gamma = \frac{(2\pi)^4}{2M}|\mathcal{M}|^2 d\Phi_n(P; p_1, ..., p_n), \tag{2.2}$$

7

where $d\Phi_n$ is an element of the n-body phase space.

In the rest frame of M, then, the momenta of the three daughters are in one plane, and the relative orientations of the momenta are dtermined by their energies. The momenta can then be described by three Euler angles (α, β, γ), that specify the orientation of the final system. The partial decay rate can then be expressed as

$$d\Gamma = \frac{1}{(2\pi)^5} \frac{1}{16M} |\mathcal{M}|^2 dE_1 dE_2 d\alpha d(\cos\beta) d\gamma \tag{2.3}$$

or,

$$d\Gamma = \frac{1}{(2\pi)^5} \frac{1}{16M} |\mathcal{M}|^2 |\mathbf{p}_1^*||\mathbf{p}_3| dm_{12} d\Omega_1^* d\Omega_3, \tag{2.4}$$

where $|\mathbf{p}_1^*|$ and Ω_1^* are the momentum and angle of particle 1 in the rest frame of m_{12}. If the mother particle is spin 0, or if we average over the spins, then after integrating over the angles we have

$$d\Gamma = \frac{1}{(2\pi)^3} \frac{1}{8M} \overline{|\mathcal{M}|^2} dE_1 dE_2 = \frac{1}{(2\pi)^3} \frac{1}{32M^3} \overline{|\mathcal{M}|^2} dm_{12}^2 dm_{23}^2. \tag{2.5}$$

This gives the partial decay rate of the three-body decay in terms of just two variables, m_{12}^2 and m_{23}^2. These, along with m_{13}^2, make up the typical Dalitz variables, commonly seen (including this document) as s_1, s_2, s_3.

The maximum and minimum kinematic limits of m_{12}^2 are described easily by $(M - m_3)^2$ and $(m_1 + m_2)^2$, respectively, with the limits of the other Dalitz variables defined similarly.

2.5 Breit-Wigner Derivation

The basic non-relativistic scattering amplitude for an unstable excited atomic state or resonance, as a function of energy, is given by (p. 101 of Reference [24])

$$f(E) \propto \frac{1}{E - E_0 + i\Gamma/2}, \tag{2.6}$$

where E_0 is the energy of the resonance. This is the non-relativistic Breit-Wigner (BW) formula, which can be generalized to the relativistic case as

$$\frac{1}{M^2 - E^2 + iM\Gamma}, \tag{2.7}$$

where p and M are the 4-momentum and pole-mass, respectively, of the unstable particle. The cross-section σ is related to the amplitude $f(E)$ by $\sigma \propto |f(E)|^2$, and thus

$$\sigma \propto \frac{1}{(E^2 - M^2)^2 + M^2\Gamma^2}. \tag{2.8}$$

2.6 Physics at Belle

The Belle experiment is operated in Tsukuba, Japan, at the KEKB accelerator, an asymmetric electron-positron collider. It was designed to function as one of the B factories, accelerators that would produce large numbers of B mesons to investigate CP violation and refine measurements of the CKM matrix.

At e^+e^- machines, the electron and positron can annihilate to a virtual photon by the electromagnetic interaction. The final state must have the same spin as the virtual photon, so the produced state must be in the spin $(s)= 1$ triplet state. In particular, at the B factories, the process for production of bottomonium is $e^+e^- \to \gamma^* \to b\bar{b}$, where the $b\bar{b}$ must be in the $s = 1, \ell = 0$ state. The $\Upsilon(nS)$ are then the only $b\bar{b}$ resonances that can be produced directly by e^+e^- annihilation.

Belle took the majority of its data at a center-of-mass (CM) energy at the $\Upsilon(4S)$ resonance, which sits right above the $B\bar{B}$ production threshold. The branching fraction of $\Upsilon(4S) \to B\bar{B}$ is greater than 96% [23], making the $\Upsilon(4S)$ the ideal energy at which to explore B physics.

The Belle experiment took a total of 711 fb^{-1} at the $\Upsilon(4S)$ resonance, 121 fb^{-1} at the $\Upsilon(10860)$ (hereafter $\Upsilon(5S)$) resonance, ≈ 100 fb^{-1} off-resonance for continuum and scan measurements, and smaller amounts at the $\Upsilon(3S)$, $\Upsilon(2S)$, and $\Upsilon(1S)$ resonances. The scan data ran as high as the $\Upsilon(11020)$ resonance, which we will call the $\Upsilon(6S)$ here.

2.7 R, R_b, cross-sections

We define

$$R \equiv \frac{\sigma(e^+e^- \to \text{hadrons})}{\sigma(e^+e^- \to \mu^+\mu^-)}, \tag{2.9}$$

where for $E_{CM} >> m_\mu$ we expect $\sigma(e^+e^- \to \mu^+\mu^-) \approx \frac{4\pi\alpha^2}{3E_{CM}^2}$ (p. 139 of Reference [24]). By analogy, and with minor modifications, this result can be adapted for hadronic production. To account for the differences in quark physics and the strong interaction, three things must be modified.

- Replace the muon charge e with the quark charge $Q|e|$.

- Count each quark three times, for each color.

- Include effects of the strong interaction between the quark/antiquark pair.

Due to asymptotic freedom, for high energies we can neglect entirely the third item, and we can write $\frac{\sigma(e^+e^- \to \text{hadrons})}{\sigma(e^+e^- \to \mu^+\mu^-)} = 3(\sum_i Q_i^2)$ for large E_{CM}, and where the sum is over all of the quarks with $m_q < E_{CM}/2$. This approximation breaks down when $E_{CM} \approx 2m_q$, where instead we find sharp peaks related to bound $q\bar{q}$ states and their excitations. Figure 2.7 shows R in the regions of light flavor, charm, and bottom thresholds. Similarly, we define R_b to be the ratio of $b\bar{b}$ production to $\mu\mu$ production, $R_b \equiv \frac{\sigma(e^+e^- \to b\bar{b})}{\sigma(e^+e^- \to \mu^+\mu^-)}$.
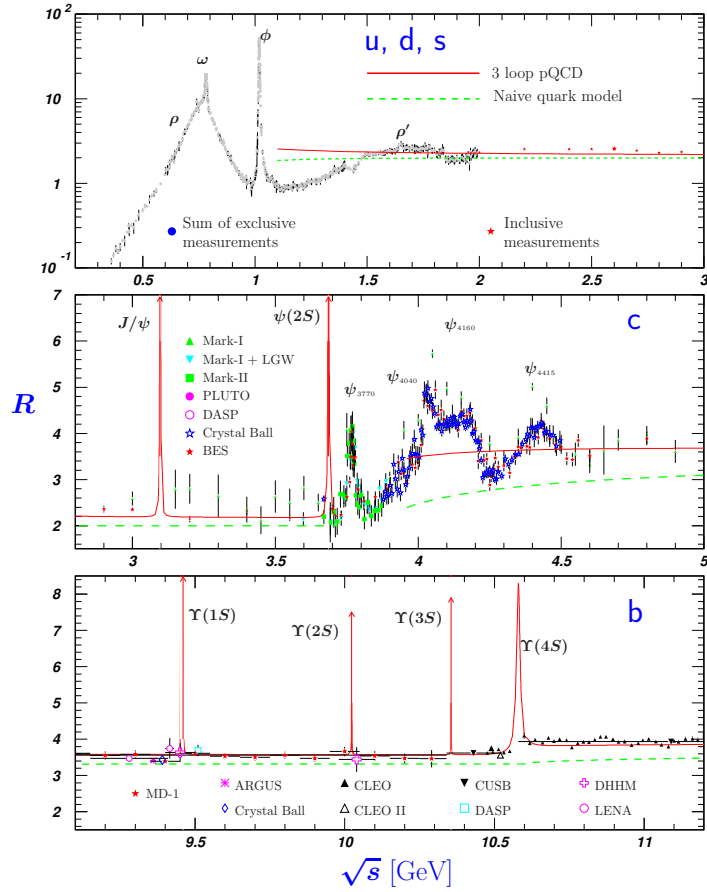
Figure 2.4: R in the regions of Light-Flavor, Charm, and Bottom thresholds. Image credit [23].

11

Chapter 3

The Belle Experiment

The Belle experiment is a high energy electron-positron collider experiment located at the High Energy Accelerator Research Organization (KEK) in Tsukuba, Japan. The detector is located at the interaction point of the KEKB accelerator. The Belle collaboration has more than 400 individual collaborators at 75 institutions in 17 countries. The main purpose of the Belle experiment, like the similar BaBar experiment, was to investigate CP (charge and parity) asymmetry and elements of the Cabibbo-Kobayashi-Maskawa (CKM) matrix in B meson decays [4]. The Belle detector took its last data in 2010 after 11 years of operation and a total accumulated luminosity 1052 fb^{-1}. The KEKB accelerator and Belle detector will be succeeded by the SuperKEKB accelerator and Belle II, with a planned 40 times improved performance.

3.1   KEKB accelerator

The KEKB accelerator is an asymmetric e^+e^- collider, designed to produce large numbers of $B\bar{B}$ meson pairs as one of the proposed so-called "B-factories." Two storage rings hold the electron (HER) and positron (LER) beams. When operated as designed, the HER beam (8.0 GeV) and LER beam (3.5 GeV) cross at an interaction point (IP) and collide with a center-of-mass (CM) energy of 10.58 GeV to produce the $\Upsilon(4S)$ meson ($M_{\Upsilon(4S)} = 10.579 \pm 1.2$

GeV [23]). When operated at the $\Upsilon(5S)$ resonance, the HER and LER beams are operated at 8.2 GeV and 3.6 GeV, respectively, for a CM energy of 10.86 GeV. The beams interact with a non-zero crossing angle of ± 11 mrad, which provides a beam separation at the interaction point which has the benefit of reducing background. The asymmetric design of the accelerator allows for a Lorentz boost of particles created at the CM. Thus, time-dependent analyses of the $B\bar{B}$ mesons produced almost at rest in the CM frame are possible, using the vertex detector.

3.2   Belle detector

The Belle detector is a multi-layer detector consisting of a silicon vertex detector (SVD), a 50-layer central drift chamber (CDC), an array of aerogel threshold Cherenkov counters (ACC), time-of-flight scintillation counters (TOF), and an electromagnetic calorimeter (ECL) comprising of CsI(Tl) crystals located inside a superconducting solenoid coil that provides a 1.5 T magnetic field. An iron flux-return located outside of the coil is used to detect K_L mesons and to identify muons (KLM). The detector is described in detail elsewhere [4].

The coordinate system is defined with the origin at the nominal interaction point. The z axis is in the direction of the magnetic field, anti-parallel to the positron beam. The x and y axes are in the horizontal and vertical directions, respectively, and the radius r is defined in the xy-plane with $r = \sqrt{x^2 + y^2}$. The azimuthal angle ϕ is subtended from the positive x axis and lies in the xy plane, and the polar angle θ is subtended from the positive z axis.

3.2.1   Beam pipe

The central part of the beam pipe is a double-wall beryllium cylinder with an inner diameter of 30 mm and a 2.5 mm gap between the inner and outer walls. The gap between the walls provides a channel for the active helium gas cooling required by the few hundred watt beam-induced heating seen near the interaction point.

3.2.2 Silicon Vertex Detector (SVD)

The Belle experiment is to observe time-dependent CP asymmetries in B meson decays, requirement measurement of z-vertex positions to a precision of ≈ 100 μm. The original SVD (SVD1) was replaced in 2003 by SVD2. SVD2 is a four-layer structure, covering a range of $16\,\mathrm{deg} < \theta < 150\,\mathrm{deg}$. Both SVDs used a double-sided silicon strip detector (DSSD) design. The four layers are at radii of 20, 43.5,70, and 88 mm from the IP, and allow for reconstruction of charged tracks from SVD hits only. The SVD2 consists of 138 DSSDs and 110592 total readout channels. It is described in detail in Reference [18].

3.2.3 Central Drift Chamber (CDC)

The CDC sits in a 1.5 T magnetic field produced by the solenoidal coil, used to identify charged particles, reconstruct trajectories, and measure their momenta.

The physics goals of the Belle experiment required a momentum resolution of $\sigma_{p_t}/p_t \approx 0.5\%\sqrt{1+p_t^2}$ (p_t in GeV) for all charged particles in $p_t >= 100$ MeV in the polar angle region of $17\,\mathrm{deg} <= \theta < 150\,\mathrm{deg}$. Since the majority of the decay particles of a B meson have momenta lower than 1 GeV, the minimization of multiple scattering is important, and a low-Z gas is desirable. A mixture of helium and ethane gas is used.

The CDC is asymmetric in z to provide the $17\,\mathrm{deg} <= \theta < 150\,\mathrm{deg}$ angular coverage. The longest wires are 2400 mm long. The inner radius is extended down 103.5 mm without walls to obtain good tracking efficiency for low-p_t tracks, and the outer radius is 874 mm. The forward and backward regions have conical shapes to clear accelerator components.

The chamber is made up of 50 cylindrical layers, each with between three and six axial or small-angle layers, and three cathode strip layers. The CDC has a total of 8400 drift cells. Individual cells are nearly square, and except for the inner three layers have a maximum distance between 8–10 mm and radial thickness of 15.5–17 mm.

When a charged particle passes through the gas, the gas is ionized and freed electrons drift to the wires in the cells, and when they connect a hit is registered in the electronics.

This way the paths of charged particles can be mapped. The path of a charged particle in a uniform magnetic field is a helix. The curvature of the helix, the slope, and the 3D coordinates are measured. The energy loss due to ionization, dE/dx, is determined using the hit amplitude recorded. The energy loss depends on the particle velocity for a given momentum, and so will vary with particle mass. The CDC can distinguish pions from kaons at momenta up to 0.8 GeV at 3σ. The CDC is described in more detail in Reference [16].

3.2.4 Aerogel Cherenkov Counter (ACC)

The aerogel Cherenkov is designed to extend the π/K separation up to momenta of 3.5 GeV. These are based on the principle that charged particles moving through material at faster than the speed of light in that material will produce Cherenkov radiation. The threshold energy for the emission of Cherenkov radiation depends on the particle velocity. The refractive indices of the aerogels in the ACC were chosen such that only pions with momenta between 1 and 4 GeV would produce light.

The ACC consists of 960 counter modules divided into 60 cells in the ϕ direction and 228 modules in 5 concentric layers for the forward end-cap of the detector. The counters are arranged in a semi-tower, pointing toward the IP. The ACC is described in more detail in Reference [17].

3.2.5 Time of Flight counters (TOF)

The TOF is used for paricle identification for particle momenta below 1.2 GeV, and can provide b-flavor tagging as well as fast timing signals for the trigger. The TOF consists of 64 modules at a radius of 1.2 m from the IP, covering an angular range $33 \deg < \theta < 121 \deg$. Each module has two trapezoidally-shaped time-of-flight counters with readout at both ends and one Trigger Scintillation Counter (TSC) with a backward readout only, separated by a radial air gap of 1.5 cm.

Scintillation light is produced by charged particles or high energy photons passing through

the plastic scintillators and is collected by photomultiplier tubes. The TOF measures time-of-flight with a resolution of 100 ps. The TOF is described in more detail in Reference [19].

3.2.6 Electromagnetic Calorimeter (ECL)

The ECL is used to detect photons from B-meson decays with high efficiency and good energy/position resolutions. Many of these photons are products of cascade decays, so are low energy and good performance below 500 MeV is important. Detection of π^0 photons requires precise measurement of the opening angle of two nearby photons, necessitating fine-grained segmentation.

Photons and electrons entering the calorimeter shower through bremsstrahlung, electron-pair production and Coulomb scattering, leaving all of the energy deposited as ionization or light in the calorimeter.

The ECL is composed of a highly-segmented array of CsI(tl) crystals with silicon photo-diode readout, installed in the 1.5 T magnetic field. The barrel section is 3.0 m in length, with an inner radius of 1.25 m and annular end-caps at $z = +2.0$ m and $z = -1.0$ m from the interaction point. Each crystal is tower-like in shape and is arranged to point almost at the IP, with a small tilt in the ϕ and θ dimensions to avoid photons escaping through the gaps between crystals. The calorimeter covers the angular region $17 \deg < \theta < 150 \deg$. The ECL is described in more detail in Reference [22].

3.2.7 KLM

The KLM is designed to identify K_Ls and muons with high efficiency for momenta greater than 600 MeV. The KLM consists of alternating layers of charged particle detectors and 4.7 cm-thick iron plates. It contains 15 detector layers and 14 iron layers arranged octagonally in the barrel region, and 14 detector layers in each of the forward and backward end-caps.

The multiple layers of particle detectors and iron allow discrimination between muons and charged hadrons based on their range and transverse scattering. Muons travel much farther with smaller deflections than the hadrons.

3.2.8 Particle identification

For charged hadron identification, a likelihood ratio is formed based on a dE/dx measurement in the CDC and the response of the ACC and TOF. Electron identification is based on a combination of dE/dx measurement, the response of the ACC, and the position, shape, and total energy deposition of the shower detected in the ECL. Muons are identified by their range and transverse scattering in the KLM.

3.2.9 Detector simulation

A GEANT-based (a CERN detector description and simulation tool) Monte Carlo (MC) simulation [9] [20] is used to model the response of the detector and determine the acceptance. The MC simulation includes run-dependent detector performance variations and background conditions.

Chapter 4

Measurement of

$\sigma(e^+e^- \to \Upsilon(nS)\pi^+\pi^-)$ vs. $\sqrt{s}$

4.1 Data Sample

Separate periods of data taking at Belle separated by experiment shutdowns and/or adjustments to the hardware, software, or other changes to detector performance are considered different experiments. The data used in this analysis span multiple different experiments (experiments 53 to 73) performed from 2006 to 2010.

Belle's 2007 $\Upsilon(nS)\pi^+\pi^-$ scan included six points of 1-2 fb^{-1} each from 10.83 GeV (below the $\Upsilon(5S)$ peak) to 11.02 GeV ($\approx \Upsilon(6S)$ peak) from experiment 61, and the analysis also used 23 fb^{-1} of $\Upsilon(5S)$ on-resonance data from experiments 43 and 53 [10]. The concurrent R_b measurement used these points and nine points of 30 pb^{-1} each over the same energy range.

The 2010 scan includes 16 new points from 10.63 GeV to 11.02 GeV at 1 fb^{-1} per point (for the $\Upsilon(nS)\pi^+\pi^-$ cross-section measurement) and an additional 61 points of 50 pb^{-1} each for the new R_b measurement, and a total of 121.4 fb^{-1} of data taken on-resonance near the $\Upsilon(5S)$ had been accumulated.

For the new $\Upsilon\pi\pi$ measurement, total data includes six points ≈ 1 fb^{-1} from 10.83 GeV

to 11.015 GeV from experiment 61, sixteen points ≈ 1 fb^{-1} from 10.63 GeV to 11.015 GeV from experiment 73, and 121.4 fb^{-1} in three points on the $\Upsilon(5S)$ resonance from experiments 43+53+67, 69, 71. Data points and luminosities are shown in Table D.1.

4.2   Integrated luminosity

The official luminosity is available run-by-run, and is based on Bhabha events. The measurement uses the process $e^+e^- \rightarrow e^+e^-$ and the Monte Carlo generator BHLUMI. The statistical error is $\approx 0.7\%$ for the relevant experiments. The official luminosities used for each scan point are summarized in Table D.1.

4.3   Event Selection

Datasets at Belle and similar experiments are very large, so different "skims" of the data with selection criteria consistent with common analyses are performed, and these skimmed datasets are what most analyses tend to begin with, to shorten analysis times. The initial measurement of $\Upsilon(5S) \rightarrow \Upsilon(nS)\pi^+\pi^-$ at Belle was performed using the tauskimA and HadronBJ skims (skims used for reconstructing τ particles and hadronic analyses, respectively. See Section A.1 for a description of these skim criteria).

These skims have criteria with complicated effects on the acceptance over the phase space of the relevant decays and resulted in particularly large inefficiencies in $\Upsilon(3S)\pi^+\pi^-$ events [10]. For the 2008 scan, the new ypipiskim was created, with only the requirements that there be two oppositely-charged lepton candidates with invariant mass $M_{l^+l^-} > 8$ GeV, which is inclusive of subsequent criteria.

Selection criteria are nearly identical to previous related analyses [11] [8] [10]. Events are reconstructed from $e^+e^- \rightarrow \Upsilon(nS)\pi^+\pi^-$, $\Upsilon(nS) \rightarrow \mu^+\mu^-$, with a $\mu^+\mu^-\pi^+\pi^-$ final state. This analysis introduces alternate cuts to remove background events from initial state radiation photon conversions. The following requirements are made for events:

19

- From ypipiskim:

  $M_{\mu^+\mu^-} > 8$ GeV.

- General criteria

  Require there to be exactly four charged tracks with transverse momentum (p_T) greater than 100 MeV.

- Track selection

  Impact parameters (distances of closest approach to the nominal e^+e^- interaction point): $|dr| < 1.0$ cm (perpendicular to the beam path) and $|dz| < 5.0$ cm (along the beam path).

- Particle identification

  - $\Upsilon(nS)$ reconstruction from $\mu^+\mu^-$

    Probability densities p_X associated with the probability that a track is of X type are determined based on readings in the detector components. The KLM is of particular importance in separating μ candidates from Ks. A likelihood ratio is defined as: $\mathcal{L}_\mu = \frac{p_\mu}{p_\mu + p_\pi + p_K}$. Muon candidates are required to have $\mathcal{L}_\mu > 0.8$ and $M_{\mu^+\mu^-} > 8$ GeV.

  - Slow pion selection

    Similarly, the likelihood that a track is an electron or positron is calculated based on readings in the CDC, ACC, and ECL, and the total $\mathcal{L}_{\text{eid}}$ is calculated: $\mathcal{L}_{\text{eid}} = \frac{p_e^{CDC} p_e^{ACC} p_e^{ECL}}{p_e^{CDC} p_e^{ACC} p_e^{ECL} + p_{\text{not }e}^{CDC} p_{\text{not }e}^{ACC} p_{\text{not }e}^{ECL}}$. Pion candidates are required to *not* be consistent with being electrons, with:

    $\mathcal{L}_{\text{eid}} < 0.1$.

- Total invariant mass of tracks

  The total invariant mass of the event is required to be consistent with the nominal $\sqrt{s}$ of the scan point, with $|M_{\mu\mu\pi\pi} - \sqrt{s}| < 200$ MeV.

- Photon conversion veto (from initial state radiation (ISR)) background reduction

1. Reject pairs of pion tracks consistent with originating from a photon, described further in Section 4.5.2.

2. We use vertex fitting to independently find the vertices the $\mu^+\mu^-$ and $\pi^+\pi^-$ originate at ($v_{\mu\mu}$, $v_{\pi\pi}$. We reject events where vertices $v_{\pi\pi}$ and $v_{\mu\mu}$ are separated in x-y ($r_{xy}^2 \equiv (x_{\mu\mu} - x_{\pi\pi})^2 + (y_{\mu\mu} - y_{\pi\pi})^2$) (see Section 4.5.3):

   (a) Veto $r_{xy} > 3$ mm for $\Upsilon(1S)$ and $\Upsilon(2S)$ events.

   (b) Veto $r_{xy} > 4.5$ mm for $\Upsilon(3S)$ events.

4.3.1 Kinematic and Vertex fits

To improve the measurement resolution of the kinematic values (of particular use in determining the Dalitz parameters of an event and the event-by-event efficiency) a series of kinematic and vertex fits is implemented.

- The $\mu^+\mu^-$ are vertex fit with the interaction point as an additional constraint. The distances of the tracks to the nominal interaction point are additional parameters to minimize.

- $M_{\mu^+\mu^-}$ constrained to $M_{\Upsilon(nS)_{PDG}}$.

- $\pi^+\pi^-$ Are fit to originate at the fitted $\mu^+\mu^-$ vertex, but are not used in determining the vertex.

Events that fall into an $\Upsilon(nS)\pi\pi$ signal box are constrained to have $M_{\mu\mu} = M(\Upsilon(nS)_{PDG})$. For each sideband, in order to produce a similarly-shaped Dalitz space, $M_{\mu\mu}$ is also constrained to the nominal $\Upsilon(nS)$ mass for the associated $\Upsilon(nS)\pi\pi$ signal.

4.4 Beam Energy Calibration

4.4.1 History

While beam orbit settings translate precisely to energy of stored beams, it was discovered early in Belle running that the true CMS collision energy at KEKB experienced a gradual wander about the "KEKB" energy, $\sqrt{s_{\text{KEKB}}}$, that was traced to hysteresis in the magnets. At the $\Upsilon(4S)$ the momentum of B mesons in $\Upsilon(4S) \to B\bar{B}$ events is a sensitive measure of $\sqrt{s}$ via the beam-constrained mass,

$$M_{\text{bc}} \equiv \sqrt{E^*_{beam}{}^2 - p^*_B{}^2}$$

where p^*_B is the momentum of the B candidate in the collison CMS and E^*_{beam} is $\sqrt{s_{\text{KEKB}}}/2$. Over the course of the Belle experiment, the CMS energy has been calibrated in groups of ~ 100 runs using the M_{bc} distribution of reconstructed B's.

At CMS energies near the $\Upsilon(10860)$, there are few $e^+e^- \to \Upsilon(10860) \to B\overline{B}$ events, so a different method is necessary. The anomalously high rate of $\Upsilon(10860) \to \Upsilon(nS)\pi^+\pi^-$ presents a serendipitous opportunity. In events $\Upsilon(10860) \to \Upsilon(1S)\pi^+\pi^-\{\Upsilon(1S) \to \mu^+\mu^-\}$, the mass difference $M_{\mu\mu\pi\pi} - M_{\mu\mu} \equiv \Delta M$ is well-resolved ($\sim 5\text{MeV}/c^2$) due to the relatively low momenta of the two pions. The event CMS energy may thus be calculated as

$$\sqrt{s_{\Upsilon\pi\pi}} \equiv \Delta M + M_{\Upsilon(1S)} \tag{4.1}$$

where $M_{\Upsilon(1S)}$ is precisely known. [23] For data sets with sufficient statistics, we thus calibrate $\sqrt{s}$ by fitting the distribution in ΔM to a double Gaussian plus second order Chebyshev polynomial. This is the official calibration method for the "$\Upsilon(5S)$" on-resonance runs, experiments 43+53, 67, 69, and 71. Each of these is more than 20 fb^{-1}, and we achieve ~ 0.5 MeV accuracy.

In [10], experiment 61 (2007 scan), the six off-resonance run energies were calibrated by taking $\sqrt{s_{\text{KEKB}}}$ and adding the difference $\sqrt{s_{\Upsilon\pi\pi}} - \sqrt{s_{\text{KEKB}}} = 2$ MeV measured in experiment 53 [12], 1.5 years earlier.

4.4.2 Experiment 73

The Experiment 73 scan in the region above the $\Upsilon(4S)$ and up to the $\Upsilon(6S)$, included sixteen additional off-resonance points of ~ 1 fb^{-1} and 61 points of ~ 50 pb^{-1}. All of these data were included in the measurement and fit for the shape of $R_b \equiv \sigma(b\bar{b})/\sigma(\mu^+\mu^-)$ by Yuan-Pao Yang. [27] A knowledge of $\sqrt{s}$ at each scan point is important for this measurement. The $\Upsilon\pi\pi$ method yields insufficient statistics for data sets of less than 1 fb^{-1}, so a different method is necessary. The calibration method chosen for this analysis is based on the mupair invariant mass, $M_{\mu\mu}$, in $e^+e^- \to \mu^+\mu^-$ events [27]. A fit of the $M_{\mu\mu}$ distribution yields a peak value, $\sqrt{s_{\mu\mu}}$. Initial state radiation (ISR) and final state radiation (FSR) result in a downward shift from the true value, $\delta_{ISR} \equiv \sqrt{s} - \sqrt{s_{\mu\mu}}$, which is determined by Monte Carlo (MC) simulation using the PHOKHARA generator. To this point the absolute accuracy of this method is limited by the calibration of the tracking and solenoidal magnetic field. The absolute calibration is determined at an on-resonance point in experiment 73 by comparing $\sqrt{s_{\mu\mu}} + \delta_{ISR}$ and $\sqrt{s_{\Upsilon\pi\pi}}$, and the observed shift $\delta_{abs} \equiv \sqrt{s_{\Upsilon\pi\pi}} - (\sqrt{s_{\mu\mu}} + \delta_{ISR})$ is applied to all of the scan points. The beam energy is thus calculated as

$$\sqrt{s_i} = \sqrt{s_{\mu\mu_i}} + \delta_{ISR,i} + \delta_{abs}. \tag{4.2}$$

4.4.3 $\quad \sqrt{s_{\Upsilon\pi\pi}}$ off the $\Upsilon(10860)$ resonance

In Reference [27], Yuan-Pao compared $\sqrt{s_i}$ and $\sqrt{s_{\Upsilon\pi\pi}}$ at seven high-luminosity ($\int \mathcal{L} \sim 1$ fb^{-1}) on- and near-$\Upsilon(10860)$ resonance points. The values are consistent for points below the $\Upsilon(10860)$ peak, but above the resonance they appear to diverge. At 10.900 GeV and 10.910 GeV the two methods differ by 4 ± 2 and 7.9 ± 2 MeV, respectively, as shown in Table 4.1 and Figure 4.1. This effect was not explored in Reference [27].

We hypothesize that the difference between $\sqrt{s_{\Upsilon\pi\pi}}$ and $\sqrt{s_i}$ may be explained by initial state radiation, i.e. $e^+e^- \to e^+e^-\gamma \to \Upsilon(10860)\gamma$, $\Upsilon(10860) \to \Upsilon(nS)\pi^+\pi^-$. Under this hypothesis, we expect the mean $\sqrt{s_{\Upsilon\pi\pi}}$ to deviate from the generated $\sqrt{s}$ at energies above the resonance as the non-radiative events become sparse relative to events radiating to the
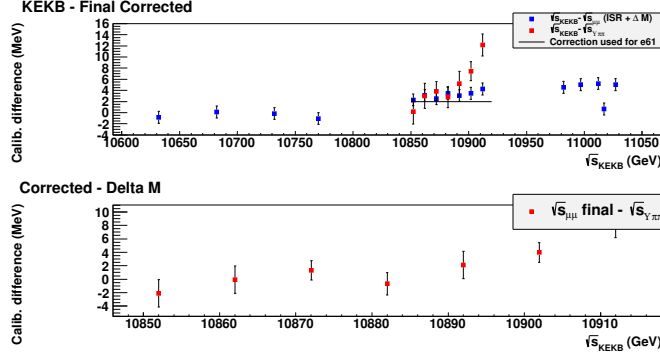
Figure 4.1: Differences between $\sqrt{s}$ values for exp 73. Top: $\sqrt{s_{KEKB}} - \sqrt{s_i}$ (blue) and $\sqrt{s_{KEKB}} - \sqrt{s_{\Upsilon\pi\pi}}$ (red). Bottom: $\sqrt{s_i} - \sqrt{s_{\Upsilon\pi\pi}}$

peak of $\Upsilon(10860)$. We performed a primitive test of this hypothesis using $e^+e^- \to \mu^+\mu^-\gamma_{ISR}$ events generated with PHOKHARA, the code used in Reference [27]. These events are generated with no beam spread. Figure 4.2 displays the generated mass $(=M_{\mu\mu})$ recoiling against ISR photon(s). The beam width is simulated by randomly smearing $M_{\mu\mu}$ by a Gaussian ($\sigma = 5$ MeV) (Figure 4.2). The smeared $M_{\mu\mu}$ distributions is then weighted by the $\Upsilon(5S)$ resonance shape (Figure 4.3), taken as a single Breit-Wigner distribution with mass and width found in Ref. [27]. This distribution is fitted with a triple Gaussian. The maximum of the distribution, derived from each fit, is plotted in Figure 4.4 as a function of $\sqrt{s}$.

Using this function as a PDF, toy experiments of 20 events each are generated to simulate a typical distribution in our data. The $\sqrt{s_{\Upsilon\pi\pi}}$ cross-check in Reference [27] is recreated by first fitting a double Gaussian to each experiment and fixing the shape parameters and relative amplitudes ($\mu_1 - \mu_2$, σ_1, σ_2/σ_1, A_1/A_2), and then floating only μ_1 and the yields in an unbinned extended maximum likelihood fit to the data.

The results are shown in Table 4.2 and Figure 4.4.

We fit $\sqrt{s} - \sqrt{s_{\Upsilon\pi\pi}}$ vs. $\sqrt{s}$ to a line:

$$\sqrt{s} - \sqrt{s_{\Upsilon\pi\pi}} = A[\sqrt{s_{\Upsilon\pi\pi}} - E_0] \tag{4.3}$$

24
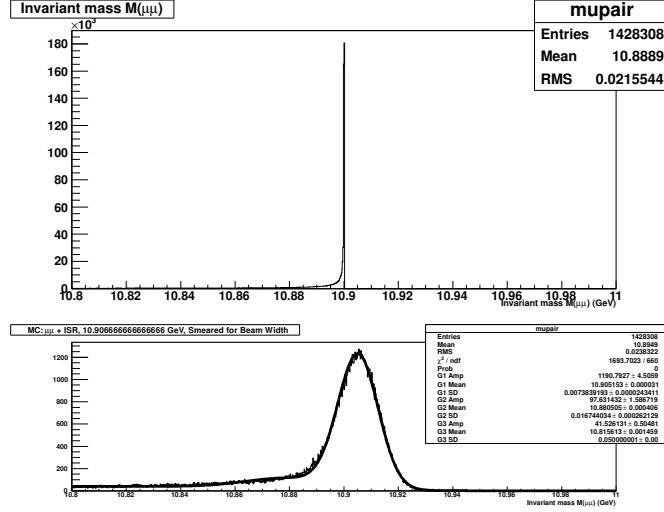
Figure 4.2: $M_{\mu\mu}$ of ISR events generated at $\sqrt{s}$=10.907 GeV, (top) generated values, (bottom) smeared for beam width.

The deviation $\sqrt{s}_{gen} - \sqrt{s}_{meas}$ grows roughly linearly with increasing energy above the resonance, which is qualitatively consistent with what is seen in data. The deficiencies of the test make quantitative statements about the consistency questionable, but we test by fitting a line to our primitive MC of $\sqrt{s}_i - \sqrt{s_{\Upsilon\pi\pi}}$ vs. $\sqrt{s}_i$, and repeat the fit to our experiment 73 results with the slope fixed to the MC result(Figure 4.4). The χ^2/dof is 13.1/6, suggesting that quantitatively our MC does not describe what is seen in data.

Still, we take this as sufficient evidence that in principle the differences seen in data between the two beam energy calibration methods could be the result of $e^+e^- \to \gamma_{ISR}\Upsilon(5S)\{\Upsilon(5S) \to \gamma\Upsilon(nS)\pi\pi\}$ being seen in the $\Upsilon\pi\pi$ measurement, and proceed with this assumption.

The final corrected $\sqrt{s_{\mu\mu}}$ energies, normalized at the resonance peak to $\sqrt{s_{\Upsilon\pi\pi}}$, will be used for experiment 73, and can be taken as consistent with the method used for the high-statistics on-resonance experiments.

Revisiting Experiment 61

Three off-resonance points from experiment 61 yielded sufficient statistics to measure $\sqrt{s_{\Upsilon\pi\pi}}$; we use the parametrization of $\sqrt{s}_i - \sqrt{s_{\Upsilon\pi\pi}}$ vs. $\sqrt{s}_{\Upsilon\pi\pi}$ obtained from the experiment 73 data
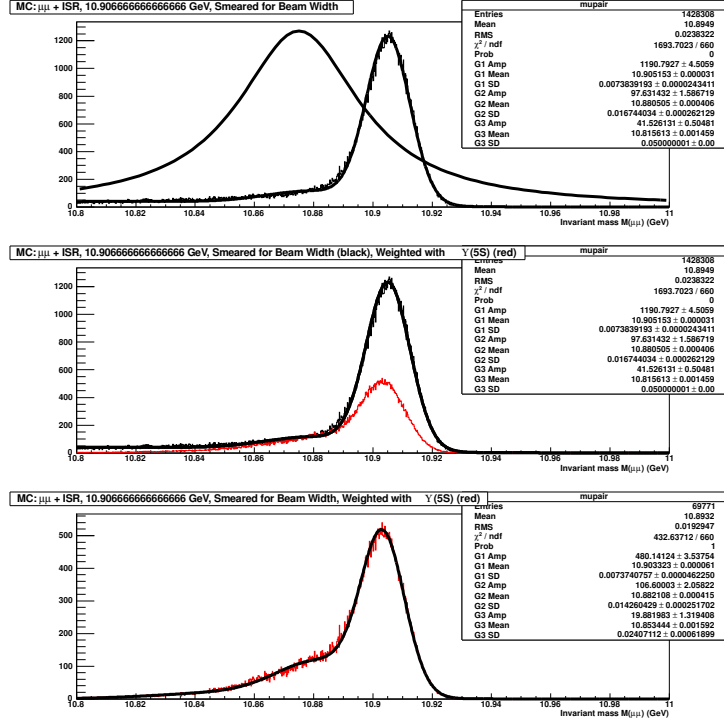
Figure 4.3: Distribution of Figure 4.2(bottom) (Histogram with fitted curve), shown with (Top) Breit-Wigner with $M = 10.875$ GeV and $\Gamma = 40$ MeV (solid line) and (Middle) same distribution weighted by the Breit-Wigner (red). (Bottom) Weighted distribution, with result of a fit to a triple-Gaussian.
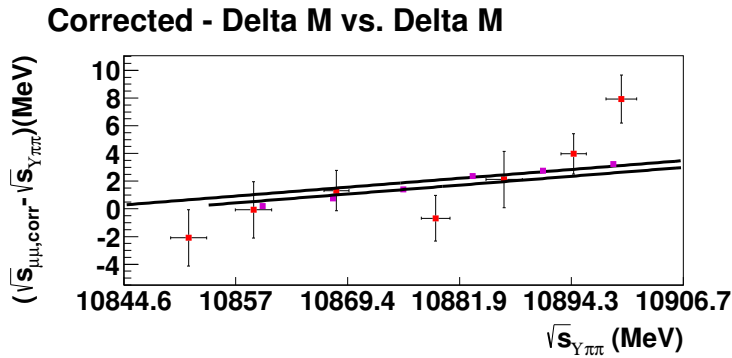
Figure 4.4: Test of ISR hypothesis of $\sqrt{s}_{\Upsilon\pi\pi}$: $\sqrt{s} - \sqrt{s_{\Upsilon\pi\pi}}$ model (magenta), and with 20-event toy experiments (red).

26

Corrected - Delta M vs. Delta M
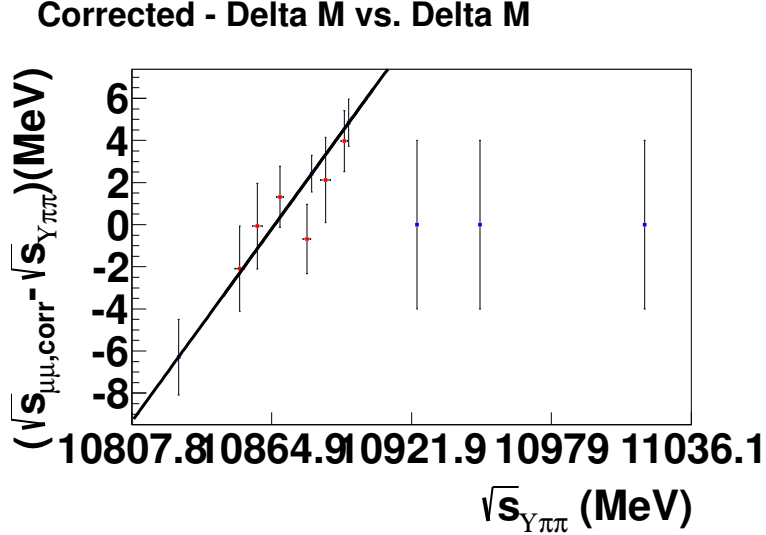
Figure 4.5: Calibration applied to e61 data points (blue) and $\sqrt{s_i} - \sqrt{s_{\Upsilon\pi\pi}}$ (red)

to apply an energy correction to these three experiment 61 points. Statistics are insufficient at the other energies, so we use $\sqrt{s_{KEKB}}$ with an uncertainty equal to the largest correction to $\sqrt{s_{KEKB}}$ used for the other three points (≈ 4 MeV) (Figure 4.5).

4.5 Initial State Radiation (ISR) Background reduction

One background component consists of ISR events where the photon converts in the beam pipe or detector ($e^+e^- \to e^+e^-\gamma \to \gamma^*\gamma\{\gamma \to e^+e^-, \gamma^* \to \mu^+\mu^-\}$), and e^+e^- fakes $\pi^+\pi^-$. Previous analyses have rejected most of these events based on the pion opening angle or a hard limit on the $M(\pi\pi)$ distribution.

The cut on $\theta_{\pi\pi}$ is not desirable due to the non-uniform effect on the efficiency across the Dalitz plot. A rejection of events with low $M_{\pi\pi}$ is similarly not ideal because it removes a piece of phase space that becomes more significant at lower scan energies. For ISR events, the "$\pi^+\pi^-$" vertex is displaced from the vertex of the $\mu^+\mu^-$ candidates, so vertexing presents another opportunity to remove these events.

$\sqrt{s_{\text{KEKB}}}$	$\sqrt{s_i}$	$\sqrt{s_{\Upsilon\pi\pi}}$
10869.0	10869.04 ± 1.1	10869.04 ± 0.97
10852.0	10849.7 ± 1.1	10851.8 ± 2.0
10862.0	10858.9 ± 1.1	10859.0 ± 2.0
10872.0	10869.5 ± 1.1	10868.2 ± 1.4
10882.0	10878.5 ± 1.1	10879.2 ± 1.6
10892.0	10888.9 ± 1.1	10886.8 ± 2.0
10902.0	10898.5 ± 1.1	10894.5 ± 1.4
10912.0	10907.7 ± 1.1	10899.8 ± 1.7

Table 4.1: Comparison of $\sqrt{s}$ methods for exp 73, in MeV: KEKB, corrected μ-pair, and $\Upsilon\pi\pi$ [27].

4.5.1   ISR Monte Carlo

The ISR Monte Carlo data are generated using EvtGen [20] with the VECTORISR model and the process $\gamma_{\text{virtual}} \to \gamma\Upsilon(nS)$. The VECTORISR model generates events of the form (virtual photon)$\to$(vector particle+photon) [25]. The generated events are passed through the detector simulation [9] as usual, and this then handles the probably of $\gamma \to e^+e^-$ and the $e^+e^- \to \pi^+\pi^-$ fake rate.

4.5.2   v0finder

The Belle analysis module v0finder tests pairs of charged tracks for consistency with $K_s \to \pi^+\pi^-$, $\Lambda \to p\pi$, $\gamma \to e^+e^-$. We veto events with $\pi^+\pi^-$ candidates identified by v0finder as originating from photons (veto KIND = 4 for the $\pi^+\pi^-$). Figure 4.6 shows the effects of rejecting $\pi^+\pi^-$ with KIND = 4 on ISR MC and signal data.

$\sqrt{s}_{\text{gen}}$ (MeV)	$\sqrt{s}_{\text{meas}}$ (MeV) $(\sqrt{s}_{\Upsilon\pi\pi})$	$\sqrt{s}_{\text{gen}} - \sqrt{s}_{\text{meas}}$
10860	10859.8±0.131917	0.214793±0.131917
10867.8	10867±0.133	0.754933±0.133
10875.6	10874.2±0.124	1.41534±0.124
10883.3	10880.9±0.15	2.36817±0.15
10891.1	10888.4±0.168	2.74962±0.168
10898.9	10895.7±0.20498	3.23186±0.20498
10906.7	10903.7±0.177	3.01634±0.177
10914.4	10911.3±0.234	3.11274±0.234
10922.2	10919.5±0.218	2.66158±0.218

Table 4.2: Low-stats MC, deviation from generated

Figure 4.6: The effects of the two photon conversion veto cuts on 121.4 fb^{-1} of $\Upsilon(5S) \to \Upsilon(1S)\pi^+\pi^-$ signal data (black) and ISR MC (red). The MC is created with many times more ISR events than expected in data. Shown are the events with no ISR vertex cuts (left), just the cut on v0type (center) and both cuts (right). Plots for $\Upsilon(2S)\pi\pi$ and $\Upsilon(3S)\pi\pi$ events are shown in Appendix E.
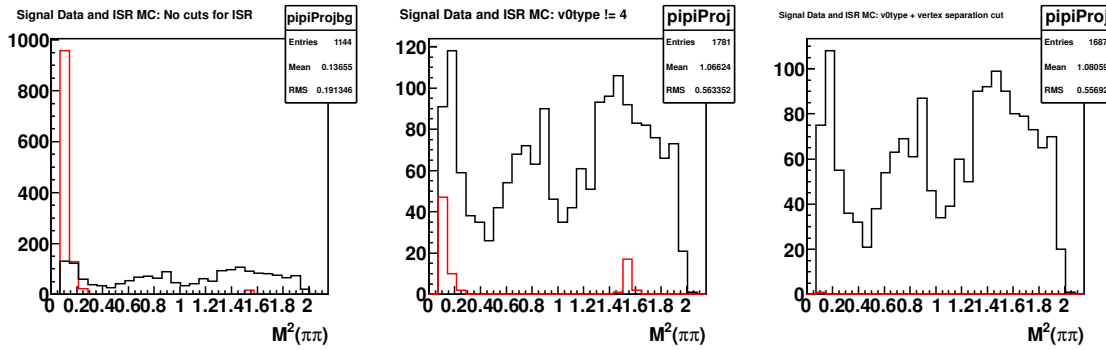
4.5.3 Vertex separation

We use vertex fitting to fit separately for the $\mu\mu$ and $\pi\pi$ vertices and then reject events based on the separation of the vertices in the x-y plane (r_{xy}), ignoring the separation in z, with

Figure 4.7: Figure of merit ($signal/\sqrt{bg}$, top), signal efficiency (center), and number of photon conversion MC events not rejected for for the vertex separation cut, for $M_{\pi\pi}^2 < 200$ MeV^2 for $\Upsilon(1S)$.
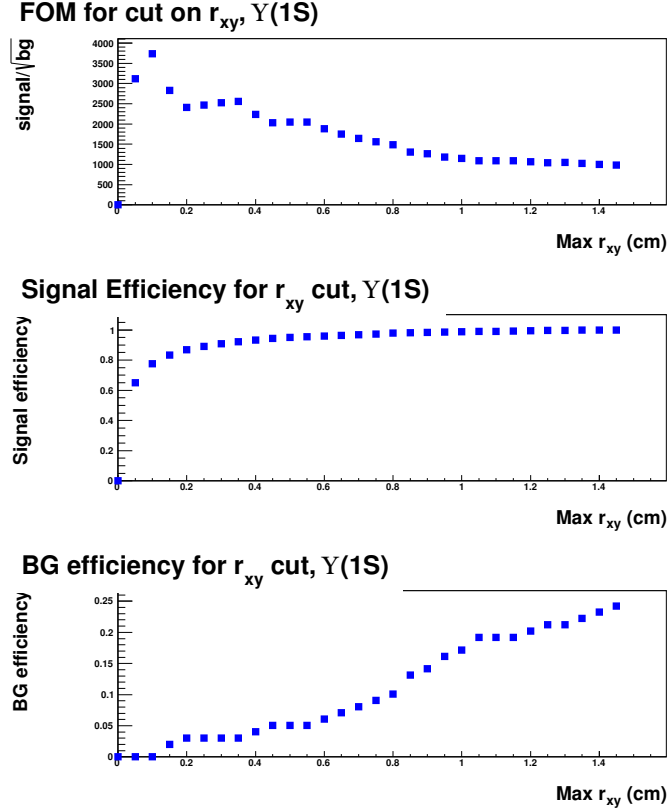
$r_{xy}^2 = (x_{\mu\mu} - x_{\pi\pi})^2 + (y_{\mu\mu} - y_{\pi\pi})^2$. Figure 4.7 shows significance (signal/$\sqrt{\text{background}}$), signal efficiency, and background efficiency as a function of the maximum allowed r_{xy} separation for the $\Upsilon(1S)\pi^+\pi^-$ decay mode ($\Upsilon(2S)$ and $\Upsilon(3S)$ modes are shown in E.7, E.8, respectively, in the appendix). We cut on $r_{xy} < 3$ mm for $\Upsilon(1S)$ and $\Upsilon(2S)$ and $r_{xy} < 4.5$ mm for $\Upsilon(3S)$ events, based on the flattening signal efficiencies and low BG acceptance at these values. Figure 4.6 shows the effects of both cuts on signal data and ISR MC events for $\Upsilon(5S) \to \Upsilon(1S)\pi\pi$ events.

The effect of the ISR cuts on signal Monte Carlo is mostly flat over the Dalitz plot, as shown in Figure 4.8.

Figure 4.8: Effects of ISR cuts on signal MC events over the Dalitz plot, $\Upsilon(1S)$ (left four) $\Upsilon(2S)$ (middle four) $\Upsilon(3S)$ (right four). Top left: Signal events with cuts. Top right: Signal events without cuts. Bottom left: Events removed by cuts. Bottom right: Removed events per total events.
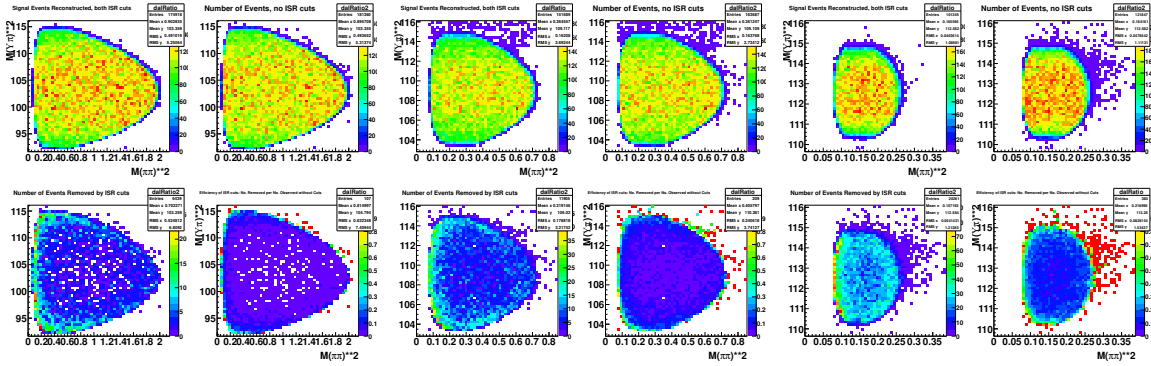
4.6 Signal and Sideband

The signal band for each mode is defined by $|\Delta M_{nom} - \Delta M_{meas}| < 25$ MeV, where $\Delta M_{meas} = M(\mu\mu\pi\pi) - M(\mu\mu)$ and $\Delta M_{nom} = \sqrt{s} - M_{\Upsilon(nS), \text{PDG}}$. Raw signal event counts are shown in Table D.1. The sidebands in ΔM are described by 50 MeV $< |\Delta M_{nom} - \Delta M_{meas}| < 100$ MeV. Raw sideband event counts are shown in Table D.2. An example event selection for experiment 69 is shown in Figure 4.9.

Figure 4.9: Signal and sideband selection for experiment 69 data (49 fb^{-1}). Solid red (blue) lines show the sideband (signal) selection windows. The dashed blue line shows the requirement $|M_{\mu\mu\pi\pi} - \sqrt{s}| < 200$ MeV. The signal boxes from top left to bottom right are associated with being $\Upsilon(3S)$, $\Upsilon(2S)$, and $\Upsilon(1S)$ events, respectively. $M_{\mu\mu}$ vs. $M_{\mu\mu\pi\pi} - M_{\mu\mu}$ (top), projection into $M_{\mu\mu\pi\pi} - M_{\mu\mu}$ (middle), and projection into $M_{\mu\mu\pi\pi} - M_{\mu\mu}$ with cut on $M_{\mu\mu\pi\pi} - \sqrt{s}$ (bottom).
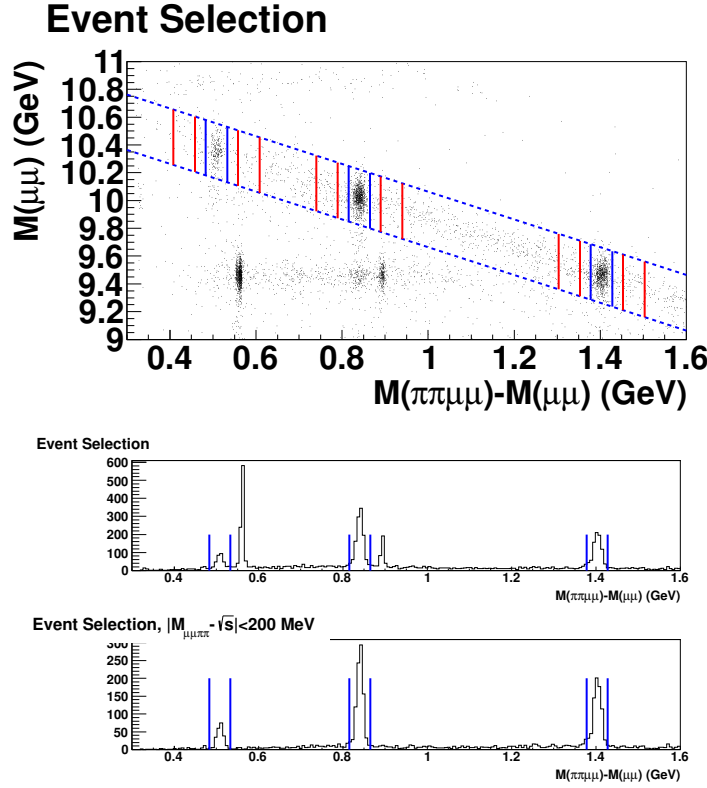
4.7 Non-ISR Background, Sideband Subtraction

Though nearly all of the photon-conversion events in Monte Carlo are removed by the ISR reduction cuts, much of the data sideband remains, with apparent structure remaining (Figure 4.10. We perform a sideband subtraction to reduce the effects of the background in the signal regions. Sidebands are taken in ΔM, are 50 MeV wide and taken from 25 MeV below and to 25 MeV above the signal region, as shown in Figure 4.9. For each mode ($\Upsilon(1S)$, $\Upsilon(2S)$, $\Upsilon(3S)$), the sideband region is twice as large as the signal region, and the event counts are scaled accordingly.

The subtraction is applied scan point by scan point after the efficiency correction is applied to both the signal and sidebands. Figure 4.10 shows Dalitz plots for the signal, individual "upper" and "lower" sidebands, and total sidebands, after both ISR cuts, for the $\Upsilon(1S)$ mode ($\Upsilon(2S)$ and $\Upsilon(3S)$ are shown in Appendix E). The sideband data for all scan points are shown in Figure 4.11.

4.8 Efficiency on the Dalitz plot

The efficiency correction used in Belle's previous $\sigma(\Upsilon\pi\pi)$ (Reference [10]) scan was based on the acceptance of Monte Carlo-simulated events, generated flat in phase space for each center-of-mass energy. To account for substructure, events were reweighted according to the $M_{\pi\pi}$ and θ_{hel} distributions observed in the analysis of $e^+e^- \to \Upsilon(5S) \to \Upsilon(nS)\pi^+\pi^-$ in experiment 53 [11].

The subsequent Dalitz plot analysis of $\Upsilon(5S) \to \Upsilon(nS)\pi^+\pi^-$ showed that there are several resonant intermediary states, including the charged Z_b resonances contributing structure in $M_{\Upsilon\pi}^2$ at significant levels [8]. The relative contributions from these and other intermediate resonances may well vary with $\sqrt{s}$, so it is important that the efficiency correction be insensitive to such variations. We correct for efficiency point-by-point over the Dalitz-space in order to obtain a more model-independent result.

Figure 4.10: Dalitz plots for $\Upsilon(5S) \to \Upsilon(1S)\pi^+\pi^-$ candidates in 121.4 fb^{-1} of $\Upsilon(5S)$ data after v0finder vertex separation cuts (in s_1 ($M^2_{\Upsilon\pi^+}$ vs. s_3 ($M^2_{\pi^+\pi^-}$). Shown are the signal region (top left), total sidebands (top right), "upper" sideband (bottom left) and "lower" sideband (bottom right). Plots for $\Upsilon(2S)$ and $\Upsilon(3S)$ are shown in Appendix E
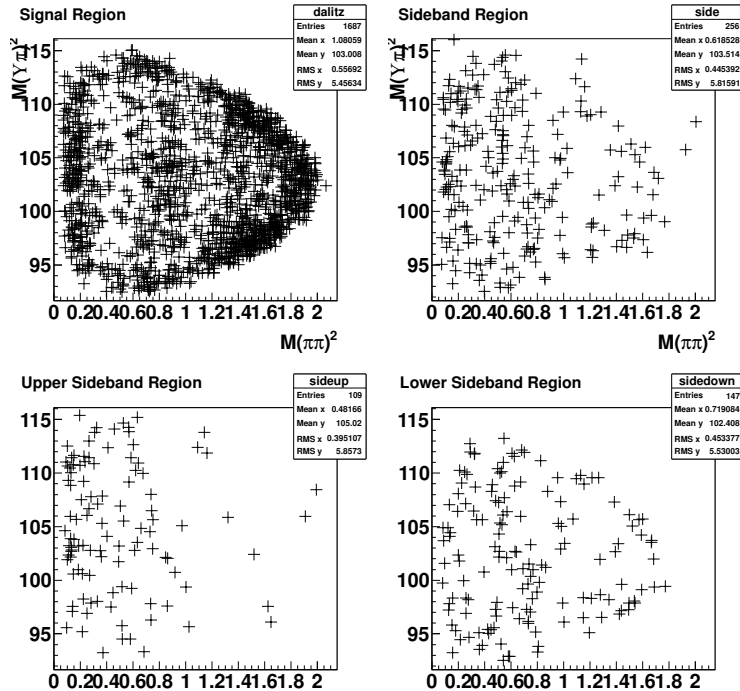
4.8.1 MC generation

We use Monte Carlo datasets to inspect the efficiency over the Dalitz plot. Events are generated with EvtGen [20] using the PHSP (flat phase space) model for $e^+e^- \to \Upsilon\pi^+\pi^-$ and VLL model for $\Upsilon \to \mu^+\mu^-$, with final state radiation via PHOTOS enabled at each step. The positron and electron beams at KEKB each have a beam width of a couple of MeV, such that there is a width of center-of-mass energies of ≈ 5 MeV. When parametrizing the efficiency function, we fix the beam width to zero in the generated Monte Carlo data.

Figure 4.11: The efficiency-corrected and luminosity-normalized cross-sections for sidebands for all scan points, for (top to bottom) $\Upsilon(1S)\pi\pi$, $\Upsilon(2S)\pi\pi$, and $\Upsilon(3S)\pi\pi$ modes.
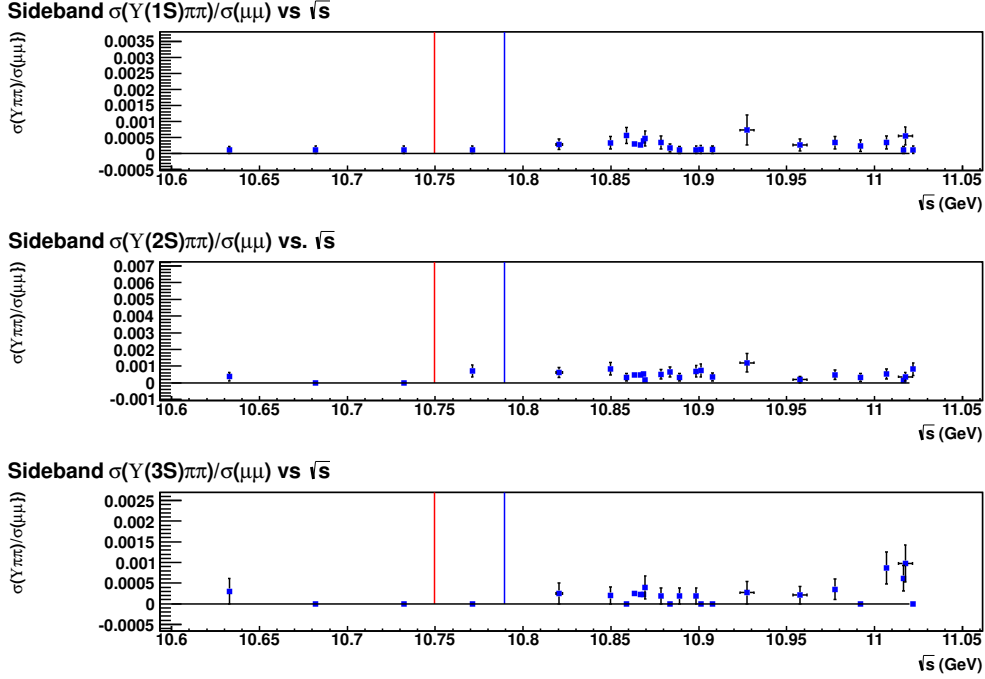
4.8.2 Parametrization of the efficiency function

To describe the efficiency we define the Dalitz variables:

$$s_1 = m^2_{\Upsilon(nS)\pi^+}, \ s_2 = m^2_{\Upsilon(nS)\pi^-}, \ s_3 = m^2_{\pi^+\pi^-} \tag{4.4}$$

We choose to use s_1 and s_2. As we found that the efficiency does not factorize easily in s_1 and s_2, we transform to $t_1 = \frac{s_1+s_2}{\sqrt{2}}$ and $t_2 = \frac{s_1-s_2}{\sqrt{2}}$ (t_1 also has the obvious relationship to the third Dalitz variable: $t_1 = (s + m^2_\Upsilon + 2m^2_\pi - s_3)/\sqrt{2}$). Over the E_{CM} range for a given scan point (Beam spread ≈ 5 MeV), we find that the efficiency is roughly constant in t_1 (and $m^2_{\pi^+\pi^-}$), while it drops with t_2 near the phase-space boundary.

We find a general form for the parametrization,

$$\epsilon(t_1, t_2, E_{CM}) = C(E_{CM}) \times (1 - e^{(t_2 - (t_2max(E_{CM}) + a_2(E_{CM}))/a_1(E_{CM}))}$$
$$\times (1 - e^{-(t_2 - (t_2min(E_{CM}) + a_3(E_{CM})))/a_1(E_{CM})}), \tag{4.5}$$

with E_{CM}-dependent parameters a_1, a_2, a_3, C, and a drop to zero at the phase space boundaries. We use fits to the Monte Carlo data to determine the appropriate parameter values.

Figure 4.12: Fit of efficiency function to MC at 10.865GeV for $\Upsilon(2S)\pi\pi$ final state.

$\chi^2/\text{ndf}: 129/207$ $\chi^2/\text{ndf}: 142/263$
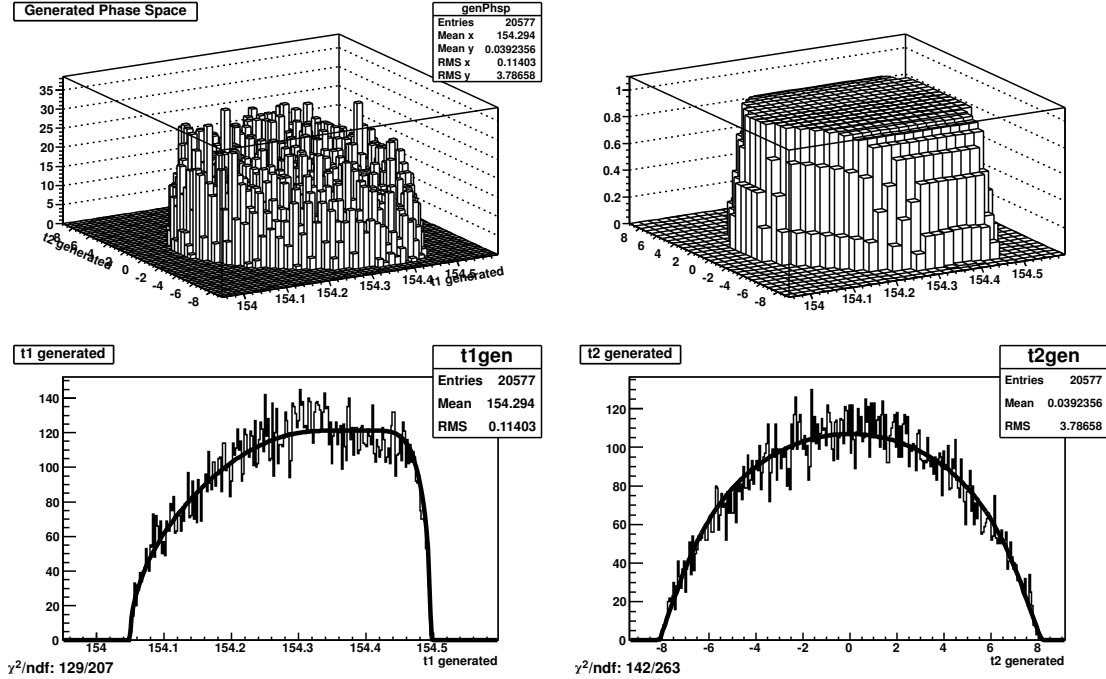
4.8.3 Efficiency parameter $\sqrt{s}$ dependence

We use the generator-level values and MC generated with no beam spread. We test the function with $\sqrt{s} = 10.63$, 10.73, 10.77, 10.86, and 11.017 GeV to determine the energy dependence of the fit parameters. We describe the parameters of the efficiency function as linear functions in $\sqrt{s}$ for all three modes (Figure 4.13) and use the energy-dependent parameters to calculate the efficiency calibration for each event.

The energy-dependencies of the parameters of the efficiency function are determined by performing unbinned maximum likelihood fits of the efficiency function to MC datasets (generated flat in phase space, with beam spread $= 0$) at a variety of energies, and for decays to each of $\Upsilon(nS)\pi^+\pi^-$. The measured center of mass energy E_{CM} is determined event-by-event via $E_{CM} = \Delta M + M_{\Upsilon_{nom}}$ where $\Delta M = M_{\mu\mu\pi\pi} - M_{\mu\mu}$. An example fit of the efficiency function to a Monte Carlo dataset with no beam width is shown in Figure 4.12.

Figure 4.13: Fitted efficiency parameters over the scan range show a largely linear dependence. ($\Upsilon(1/2/3S)$ = Blue, Magenta, Green, respectively)
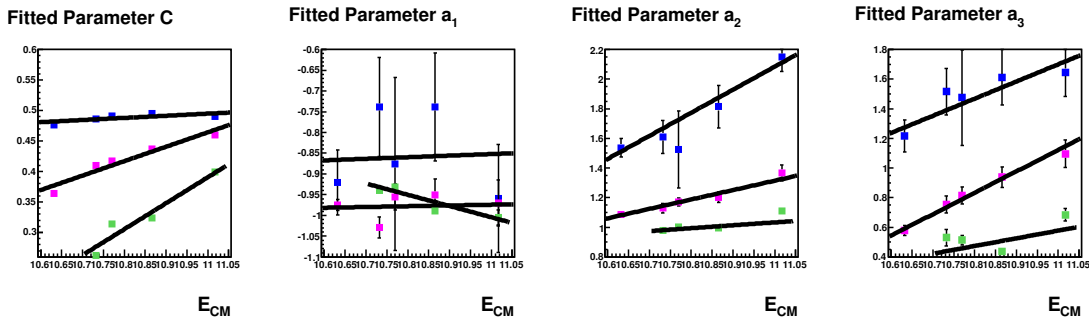
4.8.4 Tests of efficiency function

The efficiency function was parametrized using generator-level momentum/energy values with no beam spread. We perform a number of tests to check its accuracy. Using an ensemble of 50 MC datasets we verify that we recover the number of events generated within 2% for $\Upsilon(1S)$ and $\Upsilon(2S)$ decays and within 8% for $\Upsilon(3S)$ (Process D in Tables **??**, F.2, F.3).

We also check that the efficiency function is effectively model independent and accurate over the applicable $\sqrt{s}$ range. We test the $\sqrt{s}$ sensitivity by generating ensembles of events at various energies and for each final state ($\Upsilon(1S)\pi\pi$, $\Upsilon(2S)\pi\pi$, $\Upsilon(3S)\pi\pi$). These results are also shown in Tables **??**, F.2 and F.3 for $\Upsilon(1S)$, $\Upsilon(2S)$, and $\Upsilon(3S)$, respectively.

We test the model-dependence with a variety of decay processes which include purely Z_b-type resonances at the edge of phase space ("worst case", Process A) and purely phase space ("best case", Process D), as well as models with half Z_b-type and half f_n resonances (Type B) and a mix of flat phase space, Z_b, and f_n resonances (Type C). The sets are generated both with and without the beam width fixed to zero and are tested with both measured and generated kinematic values. Summaries of the decay types tested and the results are shown in Tables F.1, F.2, F.3.

In the "worst" case of 100% of $\Upsilon(nS)\pi\pi$ events coming from Z_b-type resonances, the efficiency correction overcompensates by up to 15%. We test the effects of over- or under-

correcting for the efficiency by up to 15% in the discussion of systematic errors.

4.9 Efficiency-corrected sample and cross-section measurement

The efficiency correction is applied to both the signal regions and sidebands event-by-event, where the number of efficiency corrected events $N_{cor} = \sum_{i=1}^{N_{evts}} \frac{1}{\epsilon_i}$ and ϵ_i is a function of E_{CM} and t_2.

The efficiency-corrected event yields for the signal region and sideband are shown in Tables D.3 and D.4, respectively. Measurements of the cross-section are corrected for efficiency, normalized for luminosity, scaled by the branching ratios of $\Upsilon(nS) \to \mu^+\mu^-$, and finally sideband-subtracted. The final cross-section $\sigma(\Upsilon(nS)\pi^+\pi^-)_j$ for each scan point j is calculated:

$$\sigma(\Upsilon(nS)\pi^+\pi^-)_j = \frac{\sum^{N_{sig}} \frac{1}{\epsilon_i}}{\mathcal{L}_j \times \mathcal{BR}(\Upsilon(nS) \to \mu^+\mu^-)} - \frac{\sum^{N_{sideband}} \frac{1}{\epsilon_i}}{2 * \mathcal{L}_j \times \mathcal{BR}(\Upsilon(nS) \to \mu^+\mu^-)}, \quad (4.6)$$

where ϵ_i is efficiency on the Dalitz plot at event i, $\mathcal{L}_j$ is the luminosity, and $\mathcal{BR}(\Upsilon(nS) \to \mu^+\mu^-)$ are the branching fractions as given by the PDG [23]. The cross-sections are reported in Table D.5. The fits are performed to the ratio $\sigma(\Upsilon(nS)\pi^+\pi^-/\sigma_0(\mu^+\mu^-))$, where $\sigma_0(\mu^+\mu^-)$ is the first-order cross-section for $e^+e^- \to \gamma \to \mu^+\mu^-$ in the ultrarelativistic limit, such that [23]

$$\sigma_0(\mu^+\mu^-) = \frac{4\pi\alpha^2}{3s} = \frac{86.8 \text{ nb}}{s(\text{GeV}^2)}. \quad (4.7)$$

The ratio $\sigma(\Upsilon(nS)\pi^+\pi^-/\sigma_0(\mu^+\mu^-))$ for efficiency-corrected, sideband-subtracted cross-sections is reported in Table D.6 and displayed in Figure 4.14.

Figure 4.14: $\sigma(\Upsilon(nS)\pi^+\pi^-/\sigma_0(\mu^+\mu^-)$ vs. $\sqrt{s}$ (GeV) for, $n = 1, 2, 3$, top to bottom.
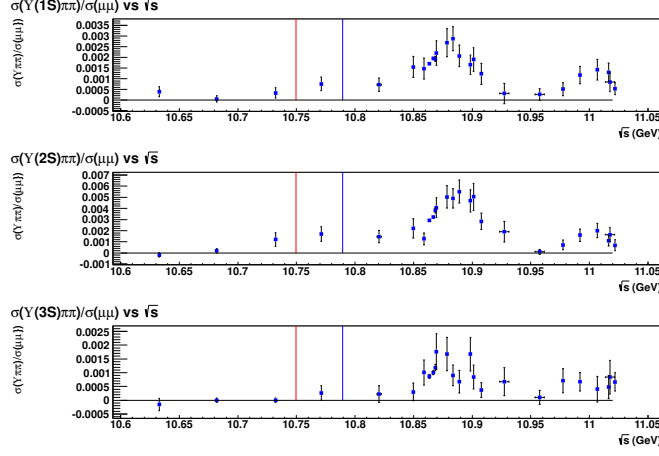
4.10 PDF

4.10.1 R_b Model, results

Our model is of the same form as the one used in both the BaBar measurement of the hadronic cross-section [7] and the most recent R_b scan by Belle [27]. This includes two Breit-Wigner functions associated with the $\Upsilon(5S)$ and $\Upsilon(6S)$ resonances, a constant non-resonant (i.e., not associated with the resonant $b\bar{b}X$ processes expected in the region) term A_R which can interfere with the resonances, and a constant non-resonant term A_{NR} which does not interfere. We take the product of this PDF with a phase-space factor (as a function of $\sqrt{s}$) to account for the thresholds of the $\Upsilon(nS)\pi^+\pi^-$ processes (9.738 GeV, 10.301 GeV, 10.634 GeV) being near or within the scan region.

$$\sigma = PHSP(\sqrt{s}) \times (|A_{NR}|^2 + |A_R + A_{5S}e^{i\phi_{5S}}BW(M_{5S}, \Gamma_{5S}) + A_{6S}e^{i\phi_{6S}}BW(M_{6S}, \Gamma_{6S})|^2) \quad (4.8)$$

Fit results are shown in Table 4.3.

Table 4.3: R_b fit results from Reference [27] (unpublished).

M_{5S} (GeV)	Γ_{5S} (GeV)	A_{5S}	ϕ_{5S} (rad)	M_{6S} (GeV)	Γ_{6S} (GeV)	A_{6S}	ϕ_{6S} (rad)	A_{NR}	A_R
10.880400 ± 0.000900	0.051 ± 0.002	0.23	2.26 ± 0.05	11.00400 ± 0.00100	0.040 ± 0.002	0.20	-1.65 ± 0.07	0.38 ± 0.01	0.42 ± 0.01

See Appendix G for a reproduction of the the R_b fit results, to test the implementation

of the PDF and other fitter machinery.

We make the assumption that the measured masses, widths, and relative phases of the two resonances will not depend on the decay channel (either $\Upsilon(nS)\pi\pi$ or R_b). For all of the initial states we consider ($\Upsilon(5S)$, $\Upsilon(6S)$, $b\bar{b}$ continuum), the paths to the final states ($\Upsilon(nS)\pi\pi$, $b\bar{b}$) are very similar, since both sides of the processes have the same valence $b\bar{b}$ [28].

We make the additional assumption for the nominal fit that the only resonant contributions to the $\Upsilon(nS)\pi\pi$ cross-sections are the $\Upsilon(5S)$ and $\Upsilon(6S)$ resonances. With these two assumptions, we perform simultaneous fits with common mass, width, and phase parameters for all three $\Upsilon\pi\pi$ decay modes but allow for mode-specific A_{5S}, A_{6S}, A_{NR} and A_R.

4.10.2 Phase Space factor

The factor PHSP in the fit model, as a function of $\sqrt{s}$, is the ratio of phase-space volumes for $e^+e^- \to \Upsilon\pi\pi$ vs. $e^+e^- \to \Upsilon\gamma\gamma$, as shown for all three decay modes in Figure 4.15. That is,

$$PHSP(\sqrt{s}) = \int \cdots \mathrm{d}^3\vec{p}_{\Upsilon(nS)}\mathrm{d}^3\vec{p}_{\pi^+}\mathrm{d}^3\vec{p}_{\pi^-} / \int \cdots \mathrm{d}^3\vec{p}_{\Upsilon(nS)}\mathrm{d}^3\vec{p}_{\gamma_1}\mathrm{d}^3\vec{p}_{\gamma_2}. \qquad (4.9)$$

The PHSP factors used as a function of $\sqrt{s}$ are shown in Figure 4.15 for all three decay modes.

4.11 Fit results

4.11.1 Consistency with R_b

One of the primary motivations of this analysis is to determine whether the resonances seen in the R_b scan, what we identify as the $\Upsilon(5S)$ and $\Upsilon(6S)$, are also the sources of the $\Upsilon(nS)\pi^+\pi^-$ decays, or if there is some other state decaying to these final states as hypothesized in, amongst others, Reference [5]. With this in mind, we test the consistency of the results of the R_b fit with the $\Upsilon(nS)\pi\pi$ data. All values except for the amplitudes

Figure 4.15: Phase space volume (PHSP) vs. $\sqrt{s}$

Phase Space Factor For Υ(1S)
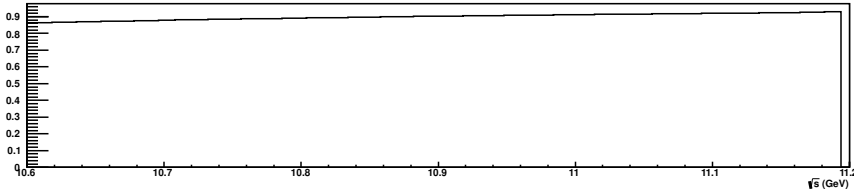
Phase Space Factor For Υ(2S)
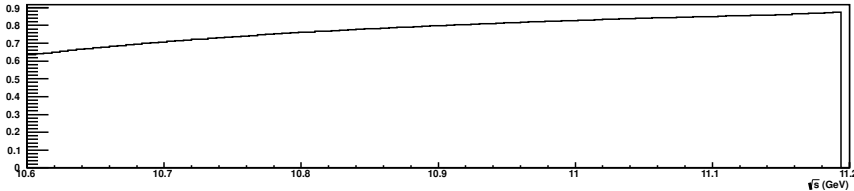
Phase Space Factor For Υ(3S)
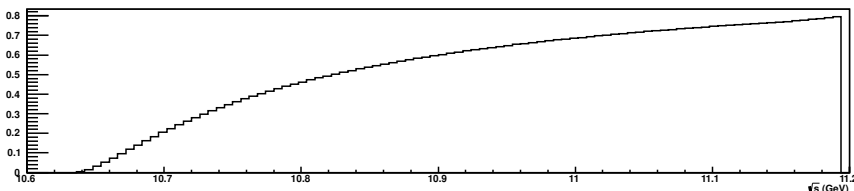
$(A_{5S,n}, A_{6S,n}, A_R, A_{NR})$ are fixed to the R_b results [27], and the fit is shown in figure 4.16. The $\chi^2/ndf = 64 / 58$ is reasonable, and shows that the $\Upsilon(nS)\pi^+\pi^-$ data are consistent with the assumption that the structures seen are the same resonances seen in the R_b distribution.

We observe that the coherent non-resonant components $(A_R(\Upsilon(nS)) = -0.002 \pm 0.003$, -0.005 ± 0.003 , 0.006 ± 0.008) are consistent with zero, while the incoherent non-resonant components $(A_{NR}(\Upsilon(nS)) = 0.013 \pm 0.004$, 0.000 ± 0.012 , -0.021 ± 0.004) are not, in this fit, i.e., that the data are consistent with $\Upsilon(nS)\pi\pi$ coming from $\Upsilon(5S)$ and $\Upsilon(6S)$ with no coherent non-resonant contribution and a small amount of incoherent $\Upsilon\pi\pi$ production, perhaps from continuum.

Though this fit prefers $A_{NR} \neq 0$, visual inspection suggests two obvious resonant structures without a strong case for the inclusion of either A_R or A_{NR}. All else being equal, we prefer the simplest model, so we consider a case with A_R and A_{NR} fixed to zero (Figure 4.17)

41

Figure 4.16: Measured $\Upsilon(nS)\pi\pi$ cross section for $\Upsilon(1S)$ (top), $\Upsilon(2S)$ (center), $\Upsilon(3S)$ (bottom). Superimposed is the fit result with shape parameters of resonances fixed to the R_b values, with $A_{5S,n}$, $A_{6S,n}$, A_R, A_{NR} floated. The points used in the previous $\Upsilon\pi\pi$ scan are shown in red. The red and blue lines show the respective $Z_b(10610)\pi$ and $Z_b(10650)\pi$ thresholds, while the magenta lines show the M_{5S} and M_{6S} used in the fit.
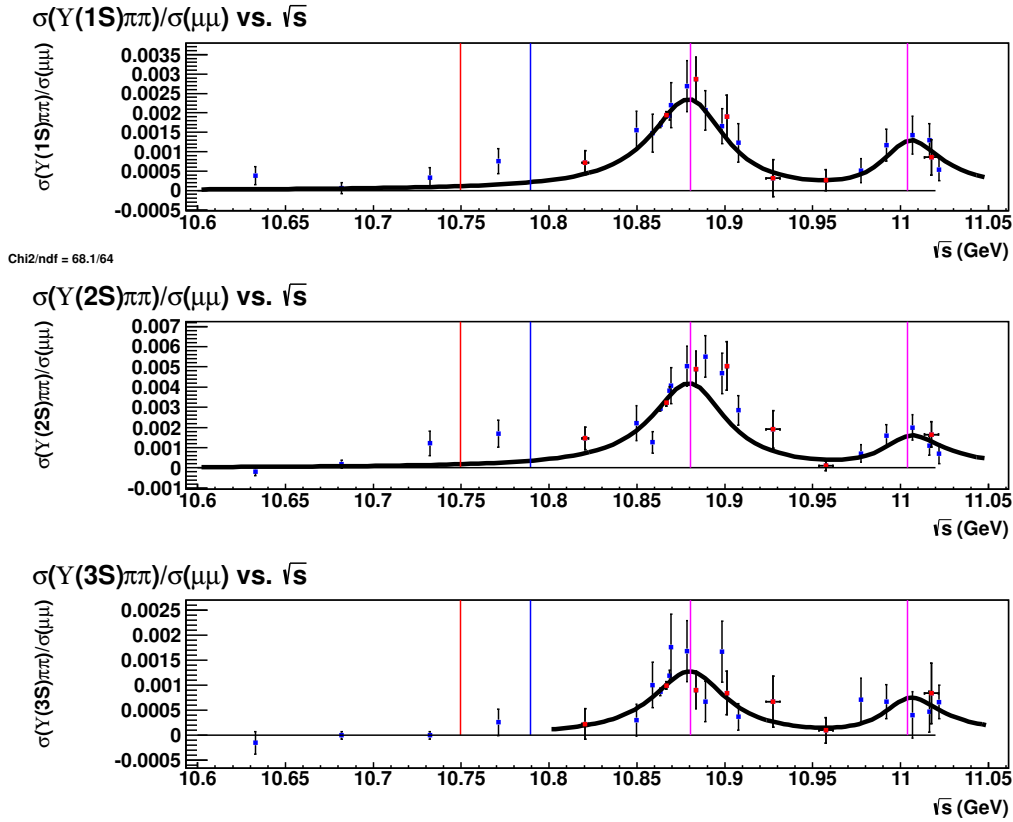
and obtain a $\chi^2/ndf = 68/64$. The $\Upsilon(nS)\pi^+\pi^-$ data are consistent with being the result of only decays from the same two interfering Breit-Wigner resonances seen in the R_b. Models with $A_R, A_{NR} \neq 0$ are considered as alternate models in the analysis of the systematic uncertainty associated with the model, in Section 4.12.1.

We then float the $\Upsilon(5S)$ mass and width. The data available around the "$\Upsilon(6S)$" resonance are sparse, so we continue to fix M_{6S}, Γ_{6S} and ϕ_{6S-5S} to the R_b results, where ϕ_{6S-5S} is the relative phase between the $\Upsilon(5S)$ and $\Upsilon(6S)$ resonances. The $\Upsilon(5S)$ parameters (M_{5S}, Γ_{5S}) and the amplitudes (A_{5S}, A_{6S}) are free parameters in the fit. The results of this fit are shown in Figure 4.18. The improvement in the fit from the R_b consistency test is not large ($\chi^2/ndf = 59/62$), but the mass ($M_{5S} = 10.8844 \pm 0.0014$) differs from the R_b result by 4 ± 1.7 MeV. The width ($\Gamma_{5S} = 0.051 \pm 0.005$) differs by 0 ± 5 MeV from the R_b value.

4.11.2   The relative $\Upsilon(5S)/\Upsilon(6S)$ phase

As described in Section 4.10.1, we expect that the relative phase between the $\Upsilon(5S)$ and $\Upsilon(6S)$ resonances should remain the same regardless of the $b\bar{b}X$ channel measured. A difference in the measured relative phase between the R_b and $\Upsilon\pi\pi$ measurements could be a hint of processes or states other than the $\Upsilon(5S)$ and $\Upsilon(6S)$. On the other hand, the interfering non-resonant component that is relatively stronger in R_b than in $\sigma(\Upsilon(ns)\pi^+\pi^-)$ could mimic a phase difference. As described in Reference [26], there are many complicated threshold effects in $\sigma(b\bar{b})$ near the scan region that may not be described by the simple non-resonant A_R and A_{NR}.

We fix the shapes of the resonances ($M_{5S,6S}$, $\Gamma_{5S,6S}$), but float ϕ_{6S-5S}, $A_{5S,n}$, $A_{6S,n}$, and keep the non-resonant amplitudes fixed to zero. The measured relative phase $\phi_{6S-5S} = -1.87 \pm 0.12$ does differ from the R_b result, but the $\chi^2/ndf = 65 / 63$ is not a statistically significant improvement. The fit is shown in Figure 4.19.

Figure 4.17: Measured $\Upsilon(nS)\pi\pi$ cross section for $\Upsilon(1S)$ (top), $\Upsilon(2S)$ (center), $\Upsilon(3S)$ (bottom). Superimposed is the fit result with shape parameters of resonances fixed to the R_b values, with $A_{5S,n}$, $A_{6S,n}$, floated, but with the non-resonant components A_R and A_{NR} fixed to zero. The points used in the previous $\Upsilon\pi\pi$ scan are shown in red. The red and blue lines show the respective $Z_b(10610)\pi$ and $Z_b(10650)\pi$ thresholds, while the magenta lines show the M_{5S} and M_{6S} used in the fit.

44
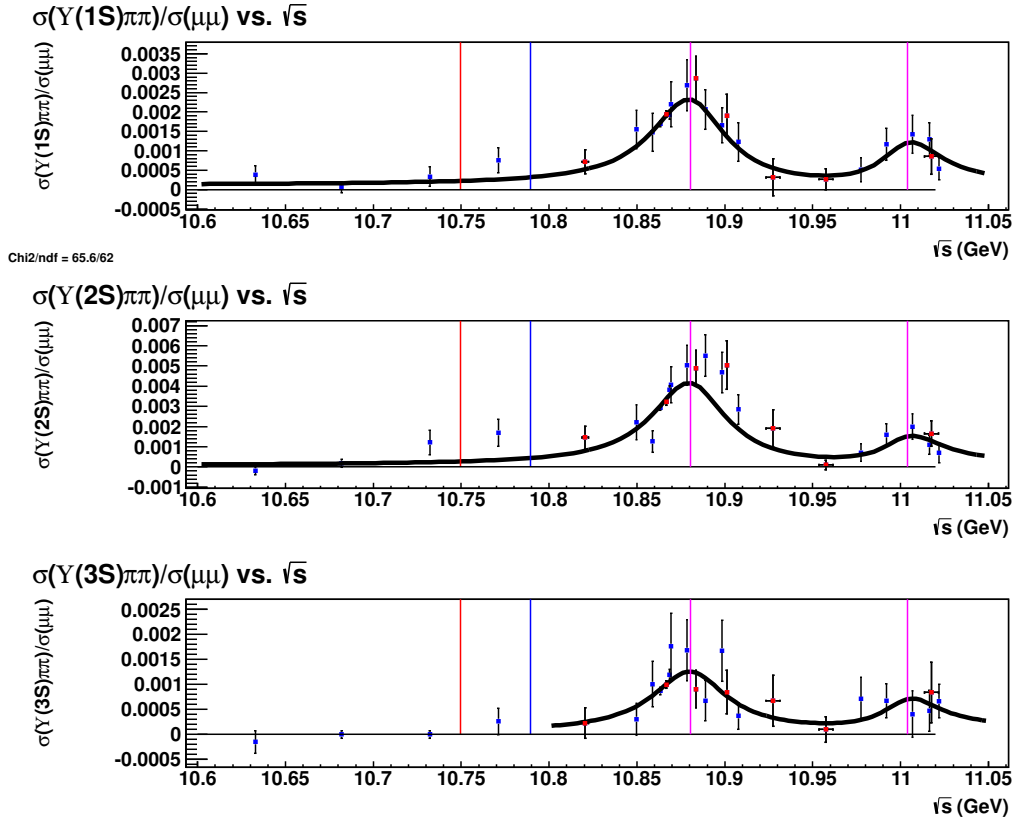
Figure 4.18: Measured $\Upsilon(nS)\pi\pi$ cross section for $\Upsilon(1S)$ (top), $\Upsilon(2S)$ (center), $\Upsilon(3S)$ (bottom). Superimposed is the fit result with floated parameters: M_{5S}, Γ_{5S}, $A_{5S,n}$, $A_{6S,n}$. A_R, A_{NR} fixed to 0. All other parameters fixed to R_b values. The points used in the previous $\Upsilon\pi\pi$ scan are shown in red. The red and blue lines show the respective $Z_b(10610)\pi$ and $Z_b(10650)\pi$ thresholds, while the magenta lines show the M_{5S} and M_{6S} used in the fit.
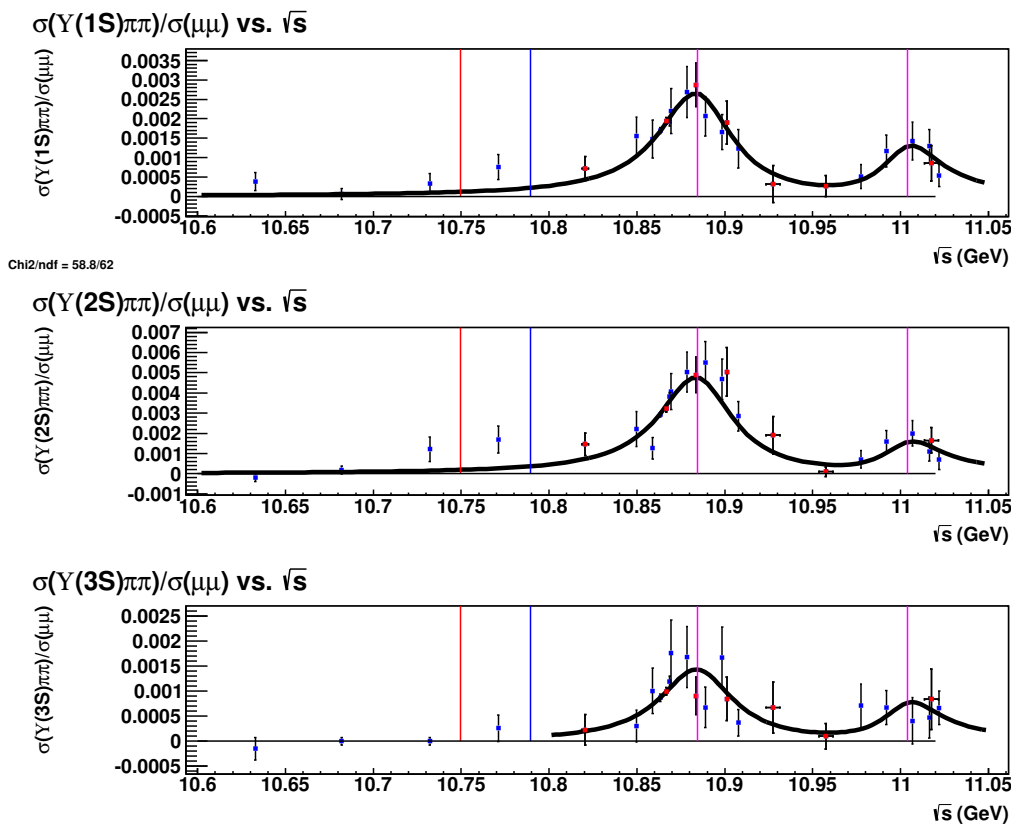
Figure 4.19: Measured $\Upsilon(nS)\pi\pi$ cross section for $\Upsilon(1S)$ (top), $\Upsilon(2S)$ (center), $\Upsilon(3S)$ (bottom). Superimposed is the fit result with floated parameters: ϕ_{6S}, A_{5S}, A_{6S}. A_R, A_{NR} are fixed to 0. All other parameters are fixed to R_b values. The points used in the previous $\Upsilon\pi\pi$ scan are shown in red. The red and blue lines show the respective $Z_b(10610)\pi$ and $Z_b(10650)\pi$ thresholds, while the magenta lines show the M_{5S} and M_{6S} used in the fit.
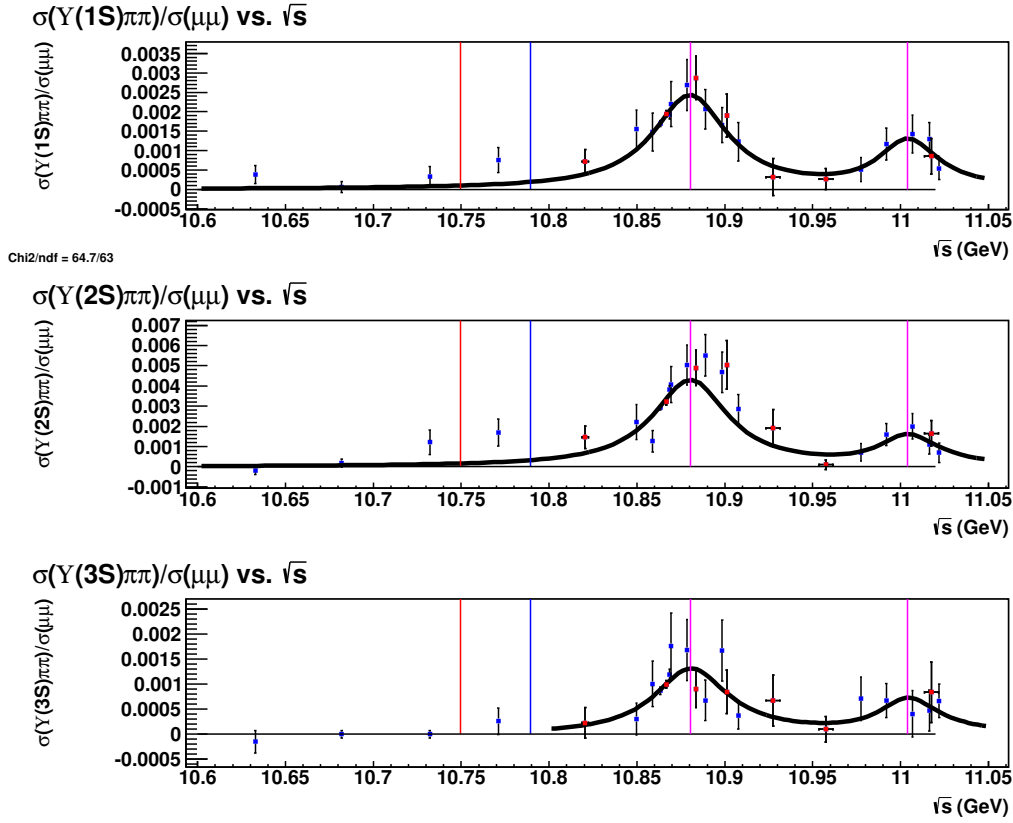
4.12 Systematics

We test for systematic errors by performing the fits with multiple fit scenarios. These include assumptions where the efficiency function under/over-corrects by different amounts starting at different energies, alternate $\sqrt{s}$ calibrations for experiment 61, different model assumptions, and different parameters floated. These are shown in Table 4.7 for a nominal fit of floating A_{5S}, A_{6S}, M_{5S} and Γ_{5S}. The largest uncertainties come from assumptions of the efficiency correction and what parameters are floated.

4.12.1 Fit Model

The R_b model includes two non-resonant components, one coherent (A_R) and one non-coherent (A_{NR}) with the two Breit-Wigner resonances. In our default fit both non-resonant components are fixed to zero. When A_R and A_{NR} are free parameters of the fit, A_R is consistent with 0, but A_{NR} deviates from 0 at $\approx 2\sigma$ for the R_b consistency fit (Section 4.11.1). As discussed in Section 4.11.1, the improvement in the χ^2/ndf for the inclusion vs. exclusion of the A_R and A_{NR} is not statistically significant, so we consider the simplest model $|BW(\Upsilon(5S)) + BW(\Upsilon(6S))|^2$ to be preferable.

We consider fit models with the A_R parameters and/or A_{NR} parameters free as reasonable alternate fit models. Our choice introduces a systematic uncertainty which we determine using four alternate fit scenarios: both A_R and A_{NR} free; $A_R = 0$ and A_{NR} free; A_R free and $A_{NR} = 0$; and (the nominal model) $A_R = 0$ and $A_{NR} = 0$.

The interfering non-resonant components (A_R) are consistent with 0 in both cases where it is free for the nominal fit (A_{5S}, A_{6S}, M_{5S} and Γ_{5S} free parameters). The non-interfering non-resonant components (A_{NR}) are inconsistent with zero at $\approx 3\sigma$. The maximum deviations of M_{5S} from the nominal fit occur with only A_R (shift of $+1$ MeV) and only A_{NR} (shift of -0.3 MeV) freed. We use these as the systematic errors associated with the fit model.

4.12.2 Efficiency Correction

As discussed in Section 4.8, the accuracy of the efficiency correction is not entirely model-independent. In extreme cases where most of the events fall near the phase space boundary (such as cases where the decay process is $\approx 100\%$ composed of $e^+e^- \to Z_b\pi \to \Upsilon\pi\pi$) the efficiency estimate can be off by up to 15%. Model-independence of the efficiency correction is important as the decay processes may change in unknown ways as a function of $\sqrt{s}$. For instance, it has been hypothesized that there could be a bottomonium-like Y_b resonance under the $\Upsilon(5S)$ around ≈ 10.89 GeV [5]. If such a particle exists and is a source of Z_b events, then the accuracy of the efficiency correction could change. The possibility of over- or under-corrections for the efficiency is treated as a systematic uncertainty. Fits are performed with different assumptions, using the area around the $\Upsilon(5S)$ as a likely place for a change in decay processes to occur:

- The efficiency correction uniformly over-corrects by 10% over the entire data range

- The efficiency correction uniformly under-corrects by 10% over the entire data range

- The efficiency correction uniformly over-corrects by 10% beginning at 10.86 GeV (just before the "$\Upsilon(10860)$")

- The efficiency correction uniformly under-corrects by 10% beginning at 10.86 GeV (just before the "$\Upsilon(10860)$")

- The efficiency correction uniformly over-corrects by 15% beginning at 10.86 GeV (just before the "$\Upsilon(10860)$")

- The efficiency correction uniformly under-corrects by 15% beginning at 10.86 GeV (just before the "$\Upsilon(10860)$")

- The efficiency correction uniformly over-corrects by 10% beginning at 10.89 GeV (just past the "$\Upsilon(10860)$")

- The efficiency correction uniformly under-corrects by 10% beginning at 10.89 GeV (just past the "$\Upsilon(10860)$")

- The efficiency correction uniformly over-corrects by 15% beginning at 10.89 GeV (just past the "$\Upsilon(10860)$")

- The efficiency correction uniformly under-corrects by 15% beginning at 10.89 GeV (just past the "$\Upsilon(10860)$")

We find that the largest differences occur with the correction of $\pm 15\%$ starting at 10.89 GeV, resulting in a shift in the fitted M_{5S} of ± 1.9 MeV.

With the default efficiency correction used in this analysis, our measurements of $\sigma(\Upsilon(nS)\pi^+\pi^-$ near the $\Upsilon(5S)$ resonance (for example, the exp43+53+67 point at 10.8667 GeV) are 1430 ± 59 nb, 2365 ± 123 nb, 733 ± 55 nb (statistical errors only) for the $\Upsilon(1S)$, $\Upsilon(2S)$ and $\Upsilon(3S)$ modes, respectively, compare well with the cross-section measurements from the full 6D amplitude analysis of $\Upsilon(5S) \to \Upsilon(nS)\pi^+\pi^-$ [14], at $1510 \pm 80 \pm 90$ nb, $2710 \pm 110 \pm 300$ nb, $970 \pm 60 \pm 110$ nb.

4.12.3 Energy Calibration

Systematic errors in the energy calibration come from two different sources, the calibration of experiment 61 and the calibration of experiment 73. Both are tested at the same time to treat the total systematic uncertainty associated with the energy calibration.

- The calibrations to $\sqrt{s}$ across the datasets have been determined in a way that should be consistent, but the previous analysis using the experiment 61 scan points used a different calibration. Additionally, three of the experiment 61 points could not be directly calibrated using the methods described in Section 4.4 above.

- The uncertainties reported for $\sqrt{s}_{\mu\mu,\,\text{corr}}$ for the experiment 73 data points include only the statistical uncertainty associated with the $M_{\mu\mu}$ peak. The calculation for the calibration also relies on $\sqrt{s}_{\Upsilon\pi\pi,\,\text{on-res}}$, however, with an uncertainty ± 1 MeV.

We generate an ensemble of 1000 different sets of $\sqrt{s}$ calibrations:

- the three un-calibrated experiment 61 points each individually shifted by a random, Gaussian-distributed amount, with a standard deviation of 4 MeV (the max shift from $\sqrt{s}_{KEKB}$ seen in the other experiment 61 points).

- the experiment 71 points uniformly shifted by a random, Gaussian-distributed amount, with a standard deviation of 1 MeV.

Five fits are performed to each dataset, each with one shape parameter (M_{5S}, Γ_{5S}, M_{6S}, Γ_{6S}, ϕ_{6S-5S} floated in addition to the standard A_{5S} and A_{6S}. The distributions of fit values for the floated shape parameter characterize the systematic uncertainty in that parameter associated with the energy calibration. A bifurcated Gaussian function is fit to each distribution, with the two standard deviations taken to be the asymmetric systematic errors. Results are shown in Table 4.4

Table 4.4: Systematic errors associated with the energy calibrations of experiment 61 and experiment 73.

M_{5S} (MeV)	Γ_{5S} (MeV)	M_{6S} (MeV)	Γ_{6S} (MeV)	ϕ_{6S-5S} (rad)
$+0.33$ / -0.34	$+0.36$ / -0.23	$+0.93$ / -1.14	$+1.24$ / -0.91	$+0.01$ / -0.01

4.12.4   Fixed parameter values

The fit results are also sensitive to what fixed values are used for the shape parameters of the resonances. In the default fits, any fixed values for the $\Upsilon(5S)$ and $\Upsilon(6S)$ shape parameters (mass, width, phase) are taken from the results of the R_b bit. The errors on these values are a source of systematic errors in this analysis. To test the effect, an ensemble of 1000 sets of correlated Gaussian numbers is generated for M_{5S}, M_{6S}, Γ_{5S}, Γ_{6S}, and ϕ_{6S-5S}, using eigen-decomposition of the correlation matrix from a fit to the R_b data.

One at a time, each parameter is freed while the others are fixed to the correlated random numbers and the fit is performed. For each floated parameter, the RMS of the distribution of fitted values is taken as the systematic error associated with the R_b fit uncertainties. The results are summarized in Table 4.5.

Table 4.5: Systematic errors associated with the uncertainty in the R_b results

M_{5S} (MeV)	Γ_{5S} (MeV)	M_{6S} (MeV)	Γ_{6S} (MeV)	ϕ_{6S-5S} (rad)
$+0.17 \ / \ -0.18$	$+0.40 \ / \ -0.13$	$+0.31 \ / \ -0.31$	$+0.93 \ / \ -0.42$	$+0.03 \ / --0.04$

4.12.5 Fit range

The model shape used here and in the R_b analyses ($|BW1e^{\imath\phi} + BW2e^{\imath\theta} + A_R|^2 + A_{NR}$) is not sufficient to describe R_b below ≈ 10.8 GeV [26]. Due to this, the previous analyses have limited their fit range to 10.8 GeV and up. The $\Upsilon(nS)\pi\pi$ cross-sections do not seem to have complicated structure below 10.8 GeV, and so our default fit uses scan points from 10.63 GeV. We include a comparison to fits made with a lower limit of 10.8 GeV.

4.12.6 Summary of Systematics

The systematic uncertainty is dominated strongly by the confidence in the efficiency function. The accuracy of the efficiency correction is ultimately limited by the measurement resolution of the Dalitz variables of a given event, but more knowledge of the changes in Dalitz structure over the scan region could be necessary to ensure accuracy. The efficiency correction in this analysis was based on an assumption of flat phase space decays, but a default assumption that the phase space stays close to what is measured at the $\Upsilon(5S)$ resonance may yield better results. A summary of the systematic errors included in this analysis is in Table 4.7.

Table 4.6: Systematics: Float M_{5S}, Γ_{5S} and Amps

Fit type	M_{5S}	Γ_{5S}	$M_{5S} - M_{5S,\mathrm{nom}}$	$\Gamma_{5S} - \Gamma_{5S,\mathrm{nom}}$
Nominal	10.8844 ± 0.0014	0.051 ± 0.005	N/A	N/A
		Efficiency		
+10% from 10.86 GeV	10.8842 ± 0.0013	0.049 ± 0.005	-0.0002 ± 0.0013	-0.001 ± 0.005
-10% from 10.86 GeV	10.8846 ± 0.0016	0.052 ± 0.006	0.0002 ± 0.0016	0.002 ± 0.006
+15% from 10.86 GeV	10.8842 ± 0.0012	0.048 ± 0.004	-0.0002 ± 0.0012	-0.002 ± 0.004
-15% from 10.86 GeV	10.8847 ± 0.0017	0.053 ± 0.007	0.0003 ± 0.0017	0.003 ± 0.007
+10% from 10.89 GeV	10.8856 ± 0.0014	0.052 ± 0.005	0.0012 ± 0.0014	0.002 ± 0.005
-10% from 10.89 GeV	10.8832 ± 0.0013	0.048 ± 0.005	-0.0012 ± 0.0013	-0.002 ± 0.005
+15% from 10.89 GeV	10.8863 ± 0.0015	0.053 ± 0.005	0.0019 ± 0.0015	0.003 ± 0.005
-15% from 10.89 GeV	10.8826 ± 0.0013	0.047 ± 0.005	-0.0018 ± 0.0013	-0.003 ± 0.005
+10% all points	10.8844 ± 0.0013	0.050 ± 0.005	-0.0000 ± 0.0013	0.000 ± 0.005
-10% all points	10.8844 ± 0.0016	0.050 ± 0.006	-0.0000 ± 0.0016	0.000 ± 0.006
		Model		
Float A_R, A_{NR}	10.8853 ± 0.0019	0.046 ± 0.005	0.0009 ± 0.0019	-0.005 ± 0.005
Float A_R	10.885 ± 0.002	0.050 ± 0.005	0.001 ± 0.002	-0.001 ± 0.005
Float A_{NR}	10.8841 ± 0.0014	0.048 ± 0.005	-0.0003 ± 0.0014	-0.003 ± 0.005

Table 4.7: Systematics: Float M_{5S}, Γ_{5S} and Amps

Source	Err M_{5S} (MeV)	Err Γ_{5S} (MeV)
Efficiency correction	± 1.9	± 3
Energy calibration	$+0.33/-0.34$	$+0.36/-0.23$
Model	$+1/-.3$	± 5
R_b fit values	$+0.17/-0.18$	$+0.40/-0.13$
Sum	± 2.0	± 3

4.13 Other considerations not included as systematic errors

4.13.1 Choice of free parameters

The fit results can be dependent on what parameters of the fits are chosen to be free or fixed. The largest contributors are the shape parameters for the "$\Upsilon(6S)$" and the relative phase between the "$\Upsilon(5S)$" and "$\Upsilon(6S)$." We repeat the fits with the following parameters freed in addition to the nominal fit (M_{5S} and Γ_{5S} free):

- M_{6S}

- Γ_{6S}

- ϕ_{6S-5S}

- M_{6S}, Γ_{6S}

- M_{6S}, ϕ_{6S-5S}

- Γ_{6S}, ϕ_{6S-5S}

- M_{6S}, Γ_{6S}, ϕ_{6S-5S}

Freeing the parameters of the second Breit-Wigner allows a shift in M_{5S} of up to +6 MeV from the nominal, and a shift in Γ_{5S} of +7 MeV. The maximum deviation occurs when M_{6S} and Γ_{6S} are both freed. Results are shown in Table 4.8.

4.14 Conclusions

We have measured the cross-section $\sigma(e^+e^- \rightarrow \Upsilon(nS)\pi^+\pi^-)$ from 10.63-11.02 GeV while using a model-insensitive efficiency correction and introducing new (to $\Upsilon(nS)\pi^+\pi^-$ decays) vertex-based selection criteria to veto the majority of the $\gamma_{\text{initial-state-radiation}} \rightarrow e^+e^-$

Table 4.8: Possible alternatives in the fit not included in systematics.

Fit type	M_{5S}	Γ_{5S}	$M_{5S} - M_{5S,\text{nom}}$	$\Gamma_{5S} - \Gamma_{5S,\text{nom}}$
Model				
no PHSP factor	10.8848 ± 0.0014	0.050 ± 0.005	0.0004 ± 0.0014	0.000 ± 0.005
Alternate fits				
Float ϕ_{5S} and Non-int	10.890 ± 0.002	0.046 ± 0.005	0.006 ± 0.002	-0.004 ± 0.005
Float ϕ_{6S} and Non-int	10.8847 ± 0.0018	0.047 ± 0.005	0.0003 ± 0.0018	-0.003 ± 0.005
Float ϕ_{5S}, ϕ_{6S} and Non-int	10.890 ± 0.002	0.046 ± 0.005	0.006 ± 0.002	-0.004 ± 0.005
Float ϕ_{6S}	10.8843 ± 0.0016	0.050 ± 0.005	-0.0001 ± 0.0016	0.000 ± 0.005
Floating $\Upsilon(6S)$ Parameters				
Float M_{6S}	10.8853 ± 0.0017	0.053 ± 0.007	0.0009 ± 0.0017	0.003 ± 0.007
Float Γ_{6S}	10.8841 ± 0.0017	0.050 ± 0.005	-0.0003 ± 0.0017	0.000 ± 0.005
Float M_{6S}, Γ_{6S}	10.891 ± 0.003	0.057 ± 0.007	0.006 ± 0.003	0.007 ± 0.007
Float M_{6S}, ϕ_{6S}	10.888 ± 0.002	0.054 ± 0.006	0.003 ± 0.002	0.004 ± 0.006
Float Γ_{6S}, ϕ_{6S}	10.8838 ± 0.0019	0.050 ± 0.005	-0.0006 ± 0.0019	0.000 ± 0.005
Float M_{6S}, Γ_{6S}, ϕ_{6S}	10.890 ± 0.004	0.054 ± 0.006	0.005 ± 0.004	0.004 ± 0.006
Sideband Subtraction				
No sideband subtraction	10.8845 ± 0.0014	0.055 ± 0.006	0.0001 ± 0.0014	0.005 ± 0.006

(ISR→photon-conversion) background. Unlike other methods used to remove these events, these vetoes are nearly flat over the Dalitz phase space.

We fit the model used in recent R_b analyses [7] [10] [27] in this scan region that includes two coherent Breit-Wigner resonances ($\Upsilon(5S)$ and $\Upsilon(6S)$), a coherent non-resonant term (A_R), and an incoherent non-resonant term (A_{NR}), but we do not find a strong case for the inclusion of the non-resonant terms in the $\Upsilon\pi\pi$ fit. Rather, the data can be described simply by two interfering Breit-Wigner resonances, with shape parameters and relative phase fixed to those of the resonances identified in the R_b analysis as the $\Upsilon(5S)$ and $\Upsilon(6S)$.

We measure the mass and width of the $\Upsilon(5S)$ resonance ($M_{5S} = 10884.4 \pm 1.4 \pm 1.6$ MeV and $\Gamma_{5S} = 50 \pm 5 \pm 3$ MeV) with a fit fixing the $\Upsilon(6S)$ parameters to the R_b results. These correspond with differences from the R_b results: $M_{5S}(\Upsilon\pi\pi) - M_{5S}(R_b) = 4.2 \pm 2.3$ MeV (1.8σ) and $\Gamma_{5S}(\Upsilon\pi\pi) - \Gamma_{5S}(R_b) = 50 \pm 5 \pm 3$ MeV ($.17\sigma$).

The data available near 11 GeV are not sufficient to perform a strongly significant mea-

surement of the $\Upsilon(6S)$ mass, width, or relative phase. A future analysis with a focus on taking additional data around 11 GeV would help pin down the relative phase ϕ_{6S-5S} and M_{6S}, which are strongly correlated in this fit.

Appendices

Appendix A

Energy Calibration for On-Res Experiments at "$\Upsilon(5S)$"

A.1 Event Selection

When the $\sqrt{s}_{\Upsilon\pi\pi}$ method was first used, the ypipi-skim was not yet available. Data from the HadronBJ and tauskim-A skims were used initially.

A.1.1 HadronA

- The event has at least 3 charged tracks ($N(\text{tracks}) \geq 3$).

- The primary vertex agrees with: $|r| < 1.5$ cm and $|z| < 3.5$ cm.

- Visible energy is greater than 40% of the beam energy ($E_{\text{vis}}/E_{\text{beam}} > 0.4$).

- The sum of ECL clusters in the MC frame is in the range $0.05 \leq \sum E^*_{\text{ECL}}/E_{\text{beam}} \leq 1.8$.

A.1.2 HadronBJ

- Hadron A is passed.

- The sum of ECL clusters in the MC frame is in the range $0.2 \leq \sum E^*_{\text{ECL}}/E_{\text{beam}} \leq 1.6$.

- At least 2 neutral clusters exist in the event.

- Average ECL energy is less than 1 GeV ($\sum E_{\text{ECL}}/N(\text{clusters}) < 1.0$ GeV).

- The sum of ECL clusters at lab frame is in the range of $\sum E_{\text{ECL}}/E_{\text{beam}} > 0.18$, and the heavy jet mass is greater than 25% of the otal visible energy ($M_{\text{heavyjet}} > 0.25 \times E_{\text{vis}}$) or is greater than 1.8 GeV/c^2.

A.1.3 tauskim-A

- *Not* in Hadron B.

- Number of charged tracks in the range $2 \leq N(\text{tracks}) \leq 8$.

- Sum of charge is in the range of $-2 \leq \sum Q(\text{tracks}) \leq 2$.

- The maximum p_T of charged tracks is greater than 0.5 GeV/c.

- Total reconstructed energy is greater than 3 GeV, or the maximum p_T of charged tracks is greater than 1.0 GeV/c

- Total energy is less than 9 GeV, or the maximum open angle between 2 charged tracks is less than 175°, or the sum of ECL energy at lab frame is in the range 2 GeV $\leq \sum E_{\text{ECL}} \leq 10$ GeV.

- At least 2 barrel clusters exist in the event, or the total track energy ($E_{\text{trk}} = \sum E_{\text{ECL}} - \sum E_\gamma$) is less than 5.3 GeV.

A.1.4 Analysis cuts

- Track selections

  For all tracks: $|dr| < 1$ cm, $|dz| < 5$ cm.

- $\Upsilon(nS)$ reconstruction

  Muon candidates are required to have a minimum muon likelihood of 0.8. Two muons

Table A.1: Beam energy calibrations to on-resonance experiments.

Experiment	$\mathcal{L}$ (fb^{-1})	N_{evts}	$\sqrt{s}_{KEKB}$ (GeV)	$\sqrt{s}_{\Upsilon\pi\pi}$
e43+e53	23.37	411	10.8710	10.8667 ± 0.0005
e67	27.22	513	10.8675	10.8661 ± 0.0006
e69	47.83	741	10.8675	10.8635 ± 0.0005
e71	22.94	443	10.8675	10.8687 ± 0.0005

with opposite charge form the $\Upsilon(1S)$ candidate, and their invariant mass must be within ± 150 MeV/c^2 of the nominal $\Upsilon(1S)$ mass.

- Slow pion selections

  A maximum electron likelihood of 0.1 is required for the charged pion candidates. The cosine of the opening angle between the π^+ and π^- is required to be less than 0.95 to suppress the $\gamma \to e^+ e^-$ background.

- Other requirements

  We require zero additional charged tracks with $p_T > 100$ MeV/c. Events should pass either the Hadron B or tauskim-A skims.

A.2   Data

The data include the on-resonance experiments taken at the $\Upsilon(5S)$ resonance ($\sqrt{s} \approx 10.870$ GeV).

A.3   Measurement of $\sqrt{s}$

The mass difference $\Delta M = M(\mu\mu\pi\pi) - M(\mu\mu)$ is measured for each experiment. This results in a clean, well-resolved signal, as shown in Figures A.1 and A.2. The peak of the signal represents the difference $\sqrt{s} - M_{nom}(\Upsilon(1S))$. The mass of the $\Upsilon(1S)$ is known to a high precision (9460.3 ± 0.26 MeV [23], and $\sqrt{s}$ is then measured by $\Delta M + M_{nom}(\Upsilon(1S))$.

Figure A.1: ΔM distributions for beam energy calibrations of experiments 43+53 (left), 67 (right)
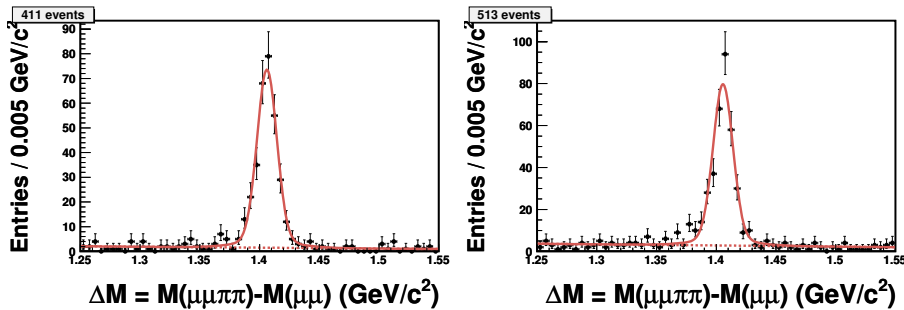
Figure A.2: ΔM distributions for beam energy calibrations of experiments 69 (left), 71 (right)
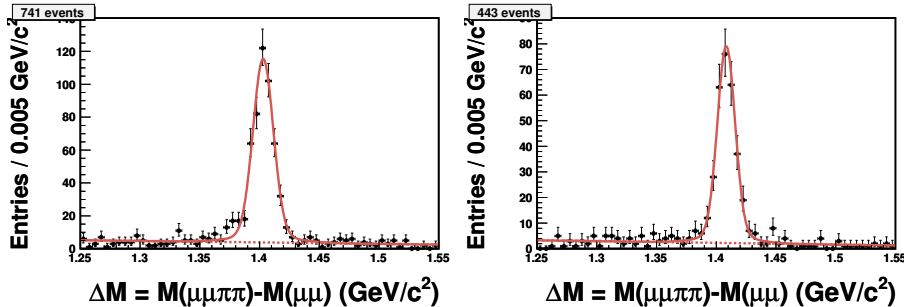
A.4 Fit results

An unbinned extended maximum likelihood fit to the data was performed, with the model of the form:

$$N_1(f \times \mathrm{Gaus}(\mu_1, \sigma) + (1 - f) \times \mathrm{Gaus}(\mu_1, a\sigma)) + N_2\mathrm{Cheb}(c). \qquad (\mathrm{A.1})$$

The double Gaussian portion is taken to be the signal, and the first-order Chebyshev polynomial the background. Results of the fits, including the final calibrated $\sqrt{s}$, are shown in Figures A.1 and A.2 and in Table A.2.

Table A.2: On-resonance $\sqrt{s}$ calibration, experiments 43, 53, 67, 69, 71.

Parameters	exp 43 + exp 53	exp 67	exp 69	exp 71
N_1	347 ± 21	386^{+24}_{-23}	630^{+62}_{-44}	357^{+26}_{-23}
N_2	55 ± 12	113 ± 17	97^{+37}_{-58}	75^{+16}_{-21}
a	$4.65^{+1.27}_{-0.73}$	$3.8^{+1.0}_{-0.7}$	$6.8^{+2.1}_{-1.4}$	$4.8^{+1.9}_{-1.0}$
f	$0.22^{+0.08}_{-0.06}$	$0.27^{+0.07}_{-0.06}$	$0.27^{+0.06}_{-0.05}$	0.25 ± 0.05
σ (GeV)	0.0075 ± 0.0007	0.0074 ± 0.0007	0.0081 ± 0.0004	0.0068 ± 0.0005
μ_1 (GeV)	1.4062 ± 0.0005	1.4058 ± 0.0005	1.4032 ± 0.0004	1.4084 ± 0.0005
$\sqrt{s}$ (GeV)	10.8667 ± 0.0006	10.8661 ± 0.0006	10.8635 ± 0.0006	10.8687 ± 0.0006

Appendix B

Consistency check with BN1073

Belle's previous R_b and $\Upsilon\pi\pi$ scans were analysed in BN1073 [12], with the results published in PRD [10]. Aside from the increase in sample size, there are many differences to account for. There are differences in efficiency calculation, reprocessing/tracking, cross-section model, and ISR-reduction cuts.

B.1   Differences in samples

There was some data loss since the previous analysis of the experiment 61 $\Upsilon\pi\pi$ scan. This resulted in an average loss $\approx 30\%$ to the available luminosity for the experiment 61 data. Table B.1 shows the loss per scan point.

The previous scan used a cut on the pion opening angle, $\cos(\theta_{lab}) < .95$, to reduce photon conversions from ISR faking $\pi^+\pi^-$. The signal and background event counts were obtained by performing Unbinned Maximum Likelihood fits of a Double Gaussian (signal) plus a Chebychev polynomial (background) to the $\Delta M_{nom} - \Delta M_{meas}$ distribution for each scan point [10].

Table B.1: Sizes of experiment 61 scan points in the original analysis and available now.

Energy (GeV)	Original (fb^{-1}) [10]	Recovered (fb^{-1})
10.83	1.74	1.16
10.88	1.89	1.27
10.9	1.46	0.87
10.93	1.18	0.67
10.96	0.99	0.85
11.02	0.88	0.85

B.2 Signal Yields

Signal and background yields were obtained in the earlier analysis by fitting a model including a double-Gaussian signal and a Chebychev polynominal background to the ΔM distributions. The current analysis subtracts an efficiency-corrected sideband yields from the efficiency-corrected signal-region events, as described above.

B.3 Efficiency calculations

The efficiency was obtained by measuring the acceptance of flat phase space Monte Carlo, weighted by the on-resonance $M_{\pi\pi}$ and θ_{hel} distributions obtained in Reference [11] [10].

B.4 Consistency

We reproduce the original analysis event selection up to the efficiency correction and obtain consistent evets/luminosity. The previous analysis produces a larger efficiency correction than the present analysis. Figure B.1 shows the efficiency-corrected experiment 61 data as reported in BN1073, using the BN1073 method as analysed now, and using the new event-by-event efficiency correction.

Figure B.1: Comparison of efficiency-corrected signal yields for experiment 61, as reported in BN1073, BN1073's method but with non-weighted flat efficiency, and with the event-by-event Dalitz-based efficiency corrections.
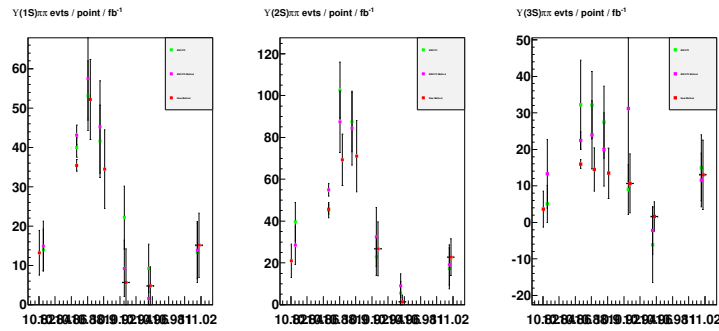
Appendix C

Alternate Fit scenarios

Fit results with a variety of other sets of floated parameters are shown in Table C.1.

Table C.1: Scan fit, various sets of parameters floated

Floated Pars	FNo	χ^2/ndf	M_{5S} (GeV)	Γ_{5S} (GeV)	A_{5S}	ϕ_{5S} Rad	M_{6S} (GeV)	Γ_{6S} (GeV)	A_{6S}	A_{6S}/A_{5S}	ϕ_{6S-5S} (Rad)	A_{nr}	A_r
$A_{5S}, A_{6S}, A_r, A_{nr}$ 1	8	67.4/62.0	10.8804	0.0510	0.0576 ± 0.0017	2.2600	11.0040	0.0400	0.047 ± 0.005	0.81 ± 0.08	-1.6500	-0.010 ± 0.004	0.0000 ± 0.0011
$A_{5S}, A_{6S}, A_r, A_{nr}$ 1	8	67.4/62.0	10.8804	0.0510	0.0816 ± 0.0016	2.2600	11.0040	0.0400	0.058 ± 0.005	0.72 ± 0.06	-1.6500	-0.010 ± 0.004	0.0000 ± 0.0011
$A_{5S}, A_{6S}, A_r, A_{nr}$ 1	8	67.4/62.0	10.8804	0.0510	0.052 ± 0.002	2.2600	11.0040	0.0400	0.042 ± 0.006	0.79 ± 0.12	-1.6500	-0.010 ± 0.004	0.0000 ± 0.0011
A_{5S}, A_{6S} 1	9	68.6/64.0	10.8804	0.0510	0.0591 ± 0.0009	2.2600	11.0040	0.0400	0.049 ± 0.004	0.83 ± 0.06	-1.6500	0	0
A_{5S}, A_{6S} 1	9	68.6/64.0	10.8804	0.0510	0.0827 ± 0.0012	2.2600	11.0040	0.0400	0.060 ± 0.005	0.73 ± 0.06	-1.6500	0	0
A_{5S}, A_{6S} 1	9	68.6/64.0	10.8804	0.0510	0.0540 ± 0.0014	2.2600	11.0040	0.0400	0.044 ± 0.006	0.81 ± 0.11	-1.6500	0	0
M_{5S}, A_{5S}, A_{6S} 1	11	59.9/63.0	10.8844 ± 0.0013	0.0510	0.0626 ± 0.0015	2.2600	11.0040	0.0400	0.050 ± 0.004	0.81 ± 0.06	-1.6500	0	0
M_{5S}, A_{5S}, A_{6S} 1	11	59.9/63.0	10.8844 ± 0.0013	0.0510	0.088 ± 0.002	2.2600	11.0040	0.0400	0.062 ± 0.005	0.70 ± 0.05	-1.6500	0	0
M_{5S}, A_{5S}, A_{6S} 1	11	59.9/63.0	10.8844 ± 0.0013	0.0510	0.0570 ± 0.0018	2.2600	11.0040	0.0400	0.045 ± 0.006	0.80 ± 0.11	-1.6500	0	0
M_{6S}, A_{5S}, A_{6S} 1	12	66.9/63.0	10.8804	0.0510	0.0595 ± 0.0009	2.2600	10.999 ± 0.003	0.0400	0.051 ± 0.004	0.85 ± 0.06	-1.6500	0	0
M_{6S}, A_{5S}, A_{6S} 1	12	66.9/63.0	10.8804	0.0510	0.0832 ± 0.0013	2.2600	10.999 ± 0.003	0.0400	0.062 ± 0.005	0.75 ± 0.06	-1.6500	0	0
M_{6S}, A_{5S}, A_{6S} 1	12	66.9/63.0	10.8804	0.0510	0.0544 ± 0.0014	2.2600	10.999 ± 0.003	0.0400	0.045 ± 0.006	0.83 ± 0.11	-1.6500	0	0
$M_{5S}, A_{5S}, A_{6S}, \phi_{6S-5S}$ 1	13	59.3/62.0	10.8848 ± 0.0015	0.0510	0.0513 ± 0.0017	2.2600	11.0040	0.0400	0.031 ± 0.004	0.60 ± 0.08	0.4 ± 0.3	0	0
$M_{5S}, A_{5S}, A_{6S}, \phi_{6S-5S}$ 1	13	59.3/62.0	10.8848 ± 0.0015	0.0510	0.075 ± 0.002	2.2600	11.0040	0.0400	0.032 ± 0.005	0.43 ± 0.06	0.4 ± 0.3	0	0
$M_{5S}, A_{5S}, A_{6S}, \phi_{6S-5S}$ 1	13	59.3/62.0	10.8848 ± 0.0015	0.0510	0.0469 ± 0.0020	2.2600	11.0040	0.0400	0.027 ± 0.006	0.58 ± 0.13	0.4 ± 0.3	0	0
$M_{5S}, M_{6S}, A_{5S}, A_{6S}, \phi_{6S-5S}$ 1	14	50.8/61.0	10.8876 ± 0.0016	0.0510	0.056 ± 0.004	2.2600	10.991 ± 0.005	0.0400	0.039 ± 0.006	0.70 ± 0.12	-0.4 ± 0.4	0	0
$M_{5S}, M_{6S}, A_{5S}, A_{6S}, \phi_{6S-5S}$ 1	14	50.8/61.0	10.8876 ± 0.0016	0.0510	0.081 ± 0.004	2.2600	10.991 ± 0.005	0.0400	0.042 ± 0.008	0.52 ± 0.10	-0.4 ± 0.4	0	0
$M_{5S}, M_{6S}, A_{5S}, A_{6S}, \phi_{6S-5S}$ 1	14	50.8/61.0	10.8876 ± 0.0016	0.0510	0.051 ± 0.003	2.2600	10.991 ± 0.005	0.0400	0.035 ± 0.007	0.69 ± 0.15	-0.4 ± 0.4	0	0
$\phi_{6S-5S}, A_{5S}, A_{6S}$ 1	17	67.0/63.0	10.8804	0.0510	0.0598 ± 0.0010	2.2600	11.0040	0.0400	0.050 ± 0.004	0.83 ± 0.06	-1.80 ± 0.11	0	0
$\phi_{6S-5S}, A_{5S}, A_{6S}$ 1	17	67.0/63.0	10.8804	0.0510	0.0836 ± 0.0014	2.2600	11.0040	0.0400	0.061 ± 0.004	0.73 ± 0.05	-1.80 ± 0.11	0	0
$\phi_{6S-5S}, A_{5S}, A_{6S}$ 1	17	67.0/63.0	10.8804	0.0510	0.0546 ± 0.0015	2.2600	11.0040	0.0400	0.044 ± 0.006	0.81 ± 0.11	-1.80 ± 0.11	0	0
$M_{5S}, M_{6S}, A_{5S}, A_{6S}$ 1	18	56.7/62.0	10.8848 ± 0.0014	0.0510	0.0635 ± 0.0016	2.2600	10.998 ± 0.004	0.0400	0.052 ± 0.004	0.83 ± 0.06	-1.6500	0	0
$M_{5S}, M_{6S}, A_{5S}, A_{6S}$ 1	18	56.7/62.0	10.8848 ± 0.0014	0.0510	0.089 ± 0.002	2.2600	10.998 ± 0.004	0.0400	0.064 ± 0.005	0.72 ± 0.06	-1.6500	0	0
$M_{5S}, M_{6S}, A_{5S}, A_{6S}$ 1	18	56.7/62.0	10.8848 ± 0.0014	0.0510	0.0578 ± 0.0019	2.2600	10.998 ± 0.004	0.0400	0.047 ± 0.006	0.81 ± 0.11	-1.6500	0	0
Floated Pars	FNo	χ^2/ndf	M_{5S} (GeV)	Γ_{5S} (GeV)	A_{5S}	ϕ_{5S} Rad	M_{6S} (GeV)	Γ_{6S} (GeV)	A_{6S}	A_{6S}/A_{5S}	ϕ_{6S-5S} (Rad)	A_{nr}	A_r
$M_{5S}, \Gamma_{5S}, A_{5S}, A_{6S}$ 1	19	59.8/62.0	10.8842 ± 0.0014	0.050 ± 0.005	0.0628 ± 0.0019	2.2600	11.0040	0.0400	0.050 ± 0.004	0.80 ± 0.06	-1.6500	0	0
$M_{5S}, \Gamma_{5S}, A_{5S}, A_{6S}$ 1	19	59.8/62.0	10.8842 ± 0.0014	0.050 ± 0.005	0.088 ± 0.003	2.2600	11.0040	0.0400	0.062 ± 0.005	0.70 ± 0.06	-1.6500	0	0
$M_{5S}, \Gamma_{5S}, A_{5S}, A_{6S}$ 1	19	59.8/62.0	10.8842 ± 0.0014	0.050 ± 0.005	0.057 ± 0.002	2.2600	11.0040	0.0400	0.045 ± 0.006	0.79 ± 0.11	-1.6500	0	0

Appendix D

Other tables

Table D.1: Raw signal event counts for $\Upsilon(1, 2, 3S)$, respectively, uncorrected for efficiency.

$\sqrt{s}$ (GeV)	Experiment	$\mathcal{L}$ fb^{-1}	N$_{\text{evts}}$ $\Upsilon(1S)$	N$_{\text{evts}}$ $\Upsilon(2S)$	N$_{\text{evts}}$ $\Upsilon(3S)$
10.6328	exp 73	0.98938	4	0	0
10.682	exp 73	0.94913	1	1	0
10.7321	exp 73	0.94596	3	5	0
10.7711	exp 73	0.95523	7	11	1
10.8205	exp 61	1.164	9	12	2
10.8497	exp 73	0.98915	14	13	2
10.8589	exp 73	0.98865	15	8	5
10.8633	exp 69	47.648	747	866	236
10.8667	exp 43+53+67	45.5228	808	856	250
10.8686	exp 71	22.938	414	515	148
10.8695	exp 73	0.9785	20	23	10
10.8785	exp 73	0.97799	22	30	9
10.8836	exp 61	1.27	31	39	6
10.8889	exp 73	0.98997	18	32	4
10.8985	exp 73	0.98332	15	28	9
10.9011	exp 61	0.873	15	27	4
10.9077	exp 73	0.98039	9	18	2
10.9275	exp 61	0.667	4	10	3
10.9575	exp 61	0.851	3	1	1
10.9775	exp 73	0.99969	6	6	5
10.9919	exp 73	0.98554	11	11	4
11.0068	exp 73	0.97647	12	14	5
11.0164	exp 73	1.05178	11	7	5
11.0175	exp 61	0.849	8	10	7
11.022	exp 73	0.982	5	7	4

Table D.2: Raw sideband event counts for $\Upsilon(1,2,3S)$, respectively, uncorrected for efficiency.

$\sqrt{s}$ (GeV)	Experiment	$\mathcal{L}$ fb^{-1}	N_{evts} $\Upsilon(1S)$	N_{evts} $\Upsilon(2S)$	N_{evts} $\Upsilon(3S)$
10.6328	exp 73	0.98938	1	2	1
10.682	exp 73	0.94913	1	0	0
10.7321	exp 73	0.94596	1	0	0
10.7711	exp 73	0.95523	1	4	0
10.8205	exp 61	1.164	3	4	1
10.8497	exp 73	0.98915	3	5	1
10.8589	exp 73	0.98865	5	2	0
10.8633	exp 69	47.648	119	129	56
10.8667	exp 43+53+67	45.5228	107	119	49
10.8686	exp 71	22.938	75	71	25
10.8695	exp 73	0.9785	4	1	2
10.8785	exp 73	0.97799	3	3	1
10.8836	exp 61	1.27	2	5	0
10.8889	exp 73	0.98997	1	2	1
10.8985	exp 73	0.98332	1	4	1
10.9011	exp 61	0.873	1	4	0
10.9077	exp 73	0.98039	1	2	0
10.9275	exp 61	0.667	3	5	1
10.9575	exp 61	0.851	2	1	1
10.9775	exp 73	0.99969	3	3	2
10.9919	exp 73	0.98554	2	2	0
11.0068	exp 73	0.97647	3	3	5
11.0164	exp 73	1.05178	1	1	4
11.0175	exp 61	0.849	4	2	5
11.022	exp 73	0.982	1	5	0

Table D.3: Signal events per fb^{-1} for $\Upsilon(1,2,3S)$, efficiency corrected.

$\sqrt{s}$ (GeV)	Experiment	$\mathcal{L}$ fb^{-1}	N$_{\text{evts}}$ $\Upsilon(1S)$	N$_{\text{evts}}$ $\Upsilon(2S)$	N$_{\text{evts}}$ $\Upsilon(3S)$
10.6328	exp 73	0.98938	8.41±4.21	0±1	0±1
10.682	exp 73	0.94913	2.18±2.18	2.78±2.78	0±1
10.7321	exp 73	0.94596	7.4±4.33	17.6±8.84	0±1
10.7711	exp 73	0.95523	15.2±5.73	29.5±8.95	4.24±4.24
10.8205	exp 61	1.164	15.8±5.28	25.3±7.34	5.68±4.02
10.8497	exp 73	0.98915	31.5±8.69	37.3±11.7	6.47±4.58
10.8589	exp 73	0.98865	32.1±8.32	20.3±7.22	16.2±7.23
10.8633	exp 69	47.648	33.6±1.38	44.8±1.72	15.9±1.07
10.8667	exp 43+53+67	45.5228	38±1.42	48.9±2.34	17.7±1.15
10.8686	exp 71	22.938	38.7±2.05	57.9±2.96	20.9±1.78
10.8695	exp 73	0.9785	44.4±10.1	58.9±12.4	31.5±9.96
10.8785	exp 73	0.97799	52±11.6	74.9±13.7	28.4±9.49
10.8836	exp 61	1.27	53.8±10.1	73.9±11.9	14.5±5.92
10.8889	exp 73	0.98997	38.5±9.13	80.2±14.4	12.3±6.15
10.8985	exp 73	0.98332	31.1±8.04	70.9±13.8	28.2±9.48
10.9011	exp 61	0.873	35.6±9.86	76.3±16.6	13.5±6.86
10.9077	exp 73	0.98039	23.3±8.76	42.5±10	5.86±4.15
10.9275	exp 61	0.667	12.2±6.24	35.1±11.7	12.8±7.49
10.9575	exp 61	0.851	7.19±4.21	2.68±2.7	3.24±3.26
10.9775	exp 73	0.99969	12.2±4.96	13.2±5.39	13.9±6.22
10.9919	exp 73	0.98554	23±6.96	24.3±7.35	10.5±5.27
11.0068	exp 73	0.97647	28.4±8.29	31.2±8.37	13.1±5.85
11.0164	exp 73	1.05178	23.9±7.54	16.2±6.37	12.2±5.46
11.0175	exp 61	0.849	20±7.37	25.2±8.37	20.7±8.09
11.022	exp 73	0.982	10.6±4.75	15.2±5.75	10.3±5.17

Table D.4: Sideband events per fb^{-1} for $\Upsilon(1, 2, 3S)$, efficiency corrected.

$\sqrt{s}$ (GeV)	Experiment	$\mathcal{L}$ fb^{-1}	N$_{\text{evts}}$ $\Upsilon(1S)$	N$_{\text{evts}}$ $\Upsilon(2S)$	N$_{\text{evts}}$ $\Upsilon(3S)$
10.6328	exp 73	0.98938	2.1±2.1	5.4±3.82	5.09±5.09
10.682	exp 73	0.94913	2.18±2.18	0±1	0±1
10.7321	exp 73	0.94596	2.19±2.19	0±1	0±1
10.7711	exp 73	0.95523	2.15±2.15	10.2±5.09	0±1
10.8205	exp 61	1.164	5.29±3.06	8.79±4.43	4.05±4.05
10.8497	exp 73	0.98915	6.19±3.57	11.9±5.32	3.26±3.26
10.8589	exp 73	0.98865	10.3±4.63	4.71±3.33	0±1
10.8633	exp 69	47.648	5.39±0.508	6.66±0.609	3.92±0.542
10.8667	exp 43+53+67	45.5228	5.03±0.506	6.57±0.627	3.54±0.514
10.8686	exp 71	22.938	7.28±0.892	7.62±0.955	3.68±0.763
10.8695	exp 73	0.9785	8.63±4.32	2.37±2.37	6.28±4.45
10.8785	exp 73	0.97799	6.26±3.61	7.17±4.14	3.09±3.09
10.8836	exp 61	1.27	3.21±2.27	9.28±4.16	0±1
10.8889	exp 73	0.98997	2.06±2.06	4.62±3.27	3.04±3.04
10.8985	exp 73	0.98332	2.09±2.09	9.67±4.85	3.1±3.1
10.9011	exp 61	0.873	2.33±2.34	10.4±5.32	0±1
10.9077	exp 73	0.98039	2.2±2.2	4.77±3.37	0±1
10.9275	exp 61	0.667	13.2±8.4	16.8±7.71	4.26±4.28
10.9575	exp 61	0.851	4.8±3.43	2.6±2.61	3.33±3.34
10.9775	exp 73	0.99969	6.07±3.5	6.64±3.83	5.48±3.88
10.9919	exp 73	0.98554	4.37±3.09	4.42±3.13	0±1
11.0068	exp 73	0.97647	6.22±3.59	7.13±4.13	13.6±6.07
11.0164	exp 73	1.05178	1.96±1.96	2.01±2.01	9.61±4.81
11.0175	exp 61	0.849	9.79±5	4.99±3.57	15.3±7.02
11.022	exp 73	0.982	2.06±2.06	11.3±5.08	0±1

Table D.5: $\sigma(\Upsilon\pi\pi)$ for three modes, efficiency corrected and background subtracted.

$\sqrt{s}$	Experiment	$\mathcal{L}$ (fb^{-1})	$\sigma(\Upsilon(1S)\pi\pi)$ (nb)	$\sigma(\Upsilon(2S)\pi\pi)$ (nb)	$\sigma(\Upsilon(3S)\pi\pi)$ (nb)
10632.8 ± 0.4	exp 73	0.989 ± 0.007	297 ± 180	-140 ± 149	-117 ± 171
10682.0 ± 0.4	exp 73	0.949 ± 0.007	44 ± 108	144 ± 149	0 ± 56
10732.1 ± 0.4	exp 73	0.946 ± 0.007	254 ± 185	914 ± 460	0 ± 56
10771.1 ± 0.3	exp 73	0.955 ± 0.007	567 ± 239	1267 ± 500	194 ± 197
10820.5 ± 1.8	exp 61	1.164 ± 0.008	532 ± 230	1086 ± 414	168 ± 226
10849.7 ± 0.4	exp 73	0.989 ± 0.007	1144 ± 365	1625 ± 636	222 ± 235
10858.9 ± 0.4	exp 73	0.989 ± 0.007	1084 ± 360	930 ± 394	741 ± 333
10863.3 ± 0.2	exp 69	47.6 ± 0.3	1247 ± 57	2149 ± 92	639 ± 52
10866.70 ± 0.19	exp 43+53+67	45.5 ± 0.3	1430 ± 59	2365 ± 123	733 ± 55
10868.6 ± 0.2	exp 71	22.94 ± 0.16	1415 ± 86	2802 ± 157	873 ± 85
10869.5 ± 0.4	exp 73	0.979 ± 0.007	1616 ± 425	2989 ± 649	1299 ± 479
10878.5 ± 0.4	exp 73	0.978 ± 0.007	1969 ± 479	3695 ± 728	1233 ± 447
10883.6 ± 0.9	exp 61	1.270 ± 0.009	2104 ± 411	3589 ± 636	664 ± 273
10888.9 ± 0.4	exp 73	0.990 ± 0.007	1513 ± 373	4033 ± 753	495 ± 299
10898.5 ± 0.4	exp 73	0.983 ± 0.007	1212 ± 330	3423 ± 736	1225 ± 446
10901.1 ± 1.1	exp 61	0.873 ± 0.006	1389 ± 403	3685 ± 883	617 ± 316
10907.7 ± 0.4	exp 73	0.980 ± 0.007	896 ± 359	2078 ± 534	269 ± 193
10928 ± 4	exp 61	0.667 ± 0.005	228 ± 347	1384 ± 668	489 ± 371
10958 ± 4	exp 61	0.851 ± 0.006	193 ± 196	72 ± 169	73 ± 185
10977.5 ± 0.4	exp 73	1.000 ± 0.007	368 ± 224	512 ± 313	510 ± 312
10991.9 ± 0.4	exp 73	0.986 ± 0.007	841 ± 294	1147 ± 398	483 ± 244
11006.8 ± 0.4	exp 73	0.976 ± 0.007	1019 ± 350	1434 ± 459	289 ± 333
11016.4 ± 0.4	exp 73	1.052 ± 0.007	926 ± 309	787 ± 338	339 ± 295
11018 ± 4	exp 61	0.849 ± 0.006	610 ± 329	1178 ± 453	599 ± 435
11022.0 ± 0.4	exp 73	0.982 ± 0.007	386 ± 200	495 ± 351	474 ± 239

Table D.6: Ratio $\sigma(\Upsilon\pi\pi)/\sigma(\mu\mu)$ for three modes, efficiency corrected and background subtracted.

$\sqrt{s}$	Experiment	$\mathcal{L}$ (fb^{-1})	$\sigma(\Upsilon(1S)\pi\pi)/\sigma(\mu\mu)$	$\sigma(\Upsilon(2S)\pi\pi)/\sigma(\mu\mu)$	$\sigma(\Upsilon(3S)\pi\pi)/\sigma(\mu\mu)$
10632.8 ± 0.4	exp 73	0.989 ± 0.007	0.0004 ± 0.0002	-0.00018 ± 0.00019	-0.0002 ± 0.0002
10682.0 ± 0.4	exp 73	0.949 ± 0.007	0.00006 ± 0.00014	0.00019 ± 0.00020	0 ± 0.0001
10732.1 ± 0.4	exp 73	0.946 ± 0.007	0.0003 ± 0.0002	0.0012 ± 0.0006	0 ± 0.0001
10771.1 ± 0.3	exp 73	0.955 ± 0.007	0.0008 ± 0.0003	0.0017 ± 0.0007	0.0003 ± 0.0003
10820.5 ± 1.8	exp 61	1.164 ± 0.008	0.0007 ± 0.0003	0.0015 ± 0.0006	0.0002 ± 0.0003
10849.7 ± 0.4	exp 73	0.989 ± 0.007	0.0016 ± 0.0005	0.0022 ± 0.0009	0.0003 ± 0.0003
10858.9 ± 0.4	exp 73	0.989 ± 0.007	0.0015 ± 0.0005	0.0013 ± 0.0005	0.0010 ± 0.0005
10863.3 ± 0.2	exp 69	47.6 ± 0.3	0.0017 ± 0.0001	0.00292 ± 0.00012	0.0009 ± 0.0001
10866.70 ± 0.19	exp 43+53+67	45.5 ± 0.3	0.0019 ± 0.0001	0.00322 ± 0.00017	0.0010 ± 0.0001
10868.6 ± 0.2	exp 71	22.94 ± 0.16	0.00193 ± 0.00012	0.0038 ± 0.0002	0.00119 ± 0.00012
10869.5 ± 0.4	exp 73	0.979 ± 0.007	0.0022 ± 0.0006	0.0041 ± 0.0009	0.0018 ± 0.0007
10878.5 ± 0.4	exp 73	0.978 ± 0.007	0.0027 ± 0.0007	0.0050 ± 0.0010	0.0017 ± 0.0006
10883.6 ± 0.9	exp 61	1.270 ± 0.009	0.0029 ± 0.0006	0.0049 ± 0.0009	0.0009 ± 0.0004
10888.9 ± 0.4	exp 73	0.990 ± 0.007	0.0021 ± 0.0005	0.0055 ± 0.0010	0.0007 ± 0.0004
10898.5 ± 0.4	exp 73	0.983 ± 0.007	0.0017 ± 0.0005	0.0047 ± 0.0010	0.0017 ± 0.0006
10901.1 ± 1.1	exp 61	0.873 ± 0.006	0.0019 ± 0.0006	0.0050 ± 0.0012	0.0008 ± 0.0004
10907.7 ± 0.4	exp 73	0.980 ± 0.007	0.0012 ± 0.0005	0.0028 ± 0.0007	0.0004 ± 0.0003
10928 ± 4	exp 61	0.667 ± 0.005	0.0003 ± 0.0005	0.0019 ± 0.0009	0.0007 ± 0.0005
10958 ± 4	exp 61	0.851 ± 0.006	0.0003 ± 0.0003	0.0001 ± 0.0002	0.0001 ± 0.0003
10977.5 ± 0.4	exp 73	1.000 ± 0.007	0.0005 ± 0.0003	0.0007 ± 0.0004	0.0007 ± 0.0004
10991.9 ± 0.4	exp 73	0.986 ± 0.007	0.0012 ± 0.0004	0.0016 ± 0.0006	0.0007 ± 0.0003
11006.8 ± 0.4	exp 73	0.976 ± 0.007	0.0014 ± 0.0005	0.0020 ± 0.0006	0.0004 ± 0.0005
11016.4 ± 0.4	exp 73	1.052 ± 0.007	0.0013 ± 0.0004	0.0011 ± 0.0005	0.0005 ± 0.0004
11018 ± 4	exp 61	0.849 ± 0.006	0.0009 ± 0.0005	0.0016 ± 0.0006	0.0008 ± 0.0006
11022.0 ± 0.4	exp 73	0.982 ± 0.007	0.0005 ± 0.0003	0.0007 ± 0.0005	0.0007 ± 0.0003

Appendix E

ISR background reduction (plots)

Figure E.1: The effects of the two vertex cuts on 121.4 fb^{-1} of $\Upsilon(5S) \to \Upsilon(nS)\pi^+\pi^-$ signal data (black) and ISR MC (red). The MC is created with many times more events than expected in signal. Shown are the events with no ISR vertex cuts (left), just the cut on v0type (center) and both cuts (right). Top to bottom: $\Upsilon(1S)$, $\Upsilon(2S)$, $\Upsilon(3S)$.
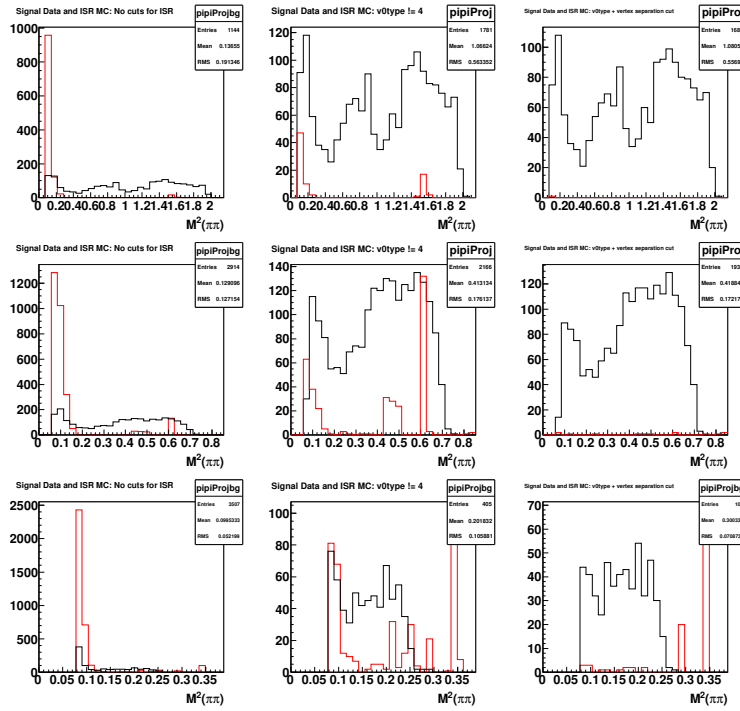
Figure E.2: Dalitz plots for 120 fb^{-1} of $\Upsilon(5S) \to \Upsilon(nS)\pi^+\pi^-$ data with no ISR reduction cuts show bands in the low $M_{\pi\pi}$ region of both signal and sidebands that represent ISR events. Shown are the signal region (top left), total sidebands (top right), "upper" sideband (bottom left) and "lower" sideband (bottom right) for $\Upsilon(1S)$ (first block of four), $\Upsilon(2S)$ (second block of four), and $\Upsilon(3S)$ (third block of four).
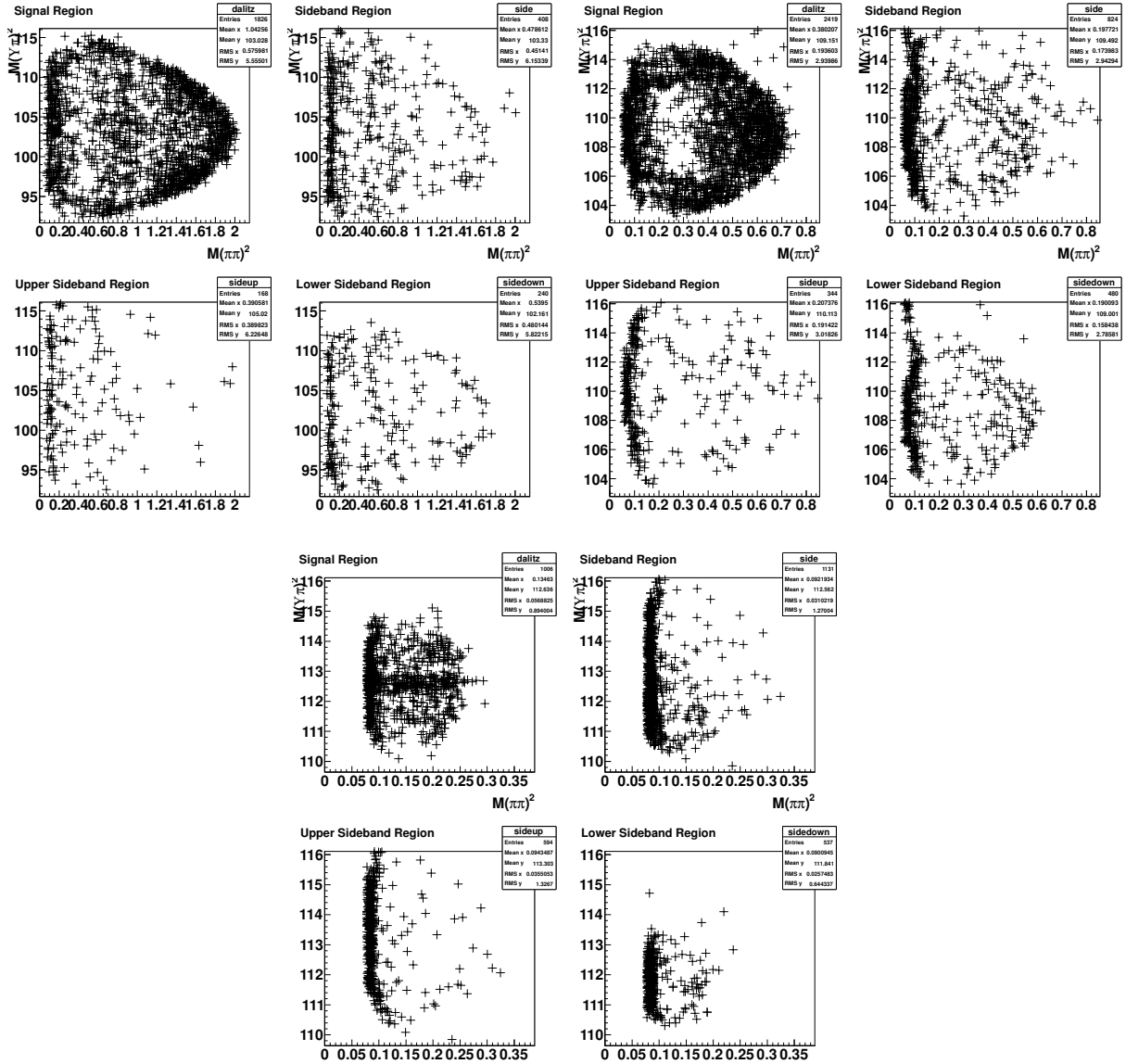
Figure E.3: Dalitz plots for 120 fb^{-1} of $\Upsilon(5S) \to \Upsilon(nS)\pi^+\pi^-$ data with the v0finder cut show large reduction in the ISR bands. Shown are the signal region (top left), total sidebands (top right), "upper" sideband (bottom left) and "lower" sideband (bottom right) for $\Upsilon(1S)$ (first block of four), $\Upsilon(2S)$ (second block of four), and $\Upsilon(3S)$ (third block of four).
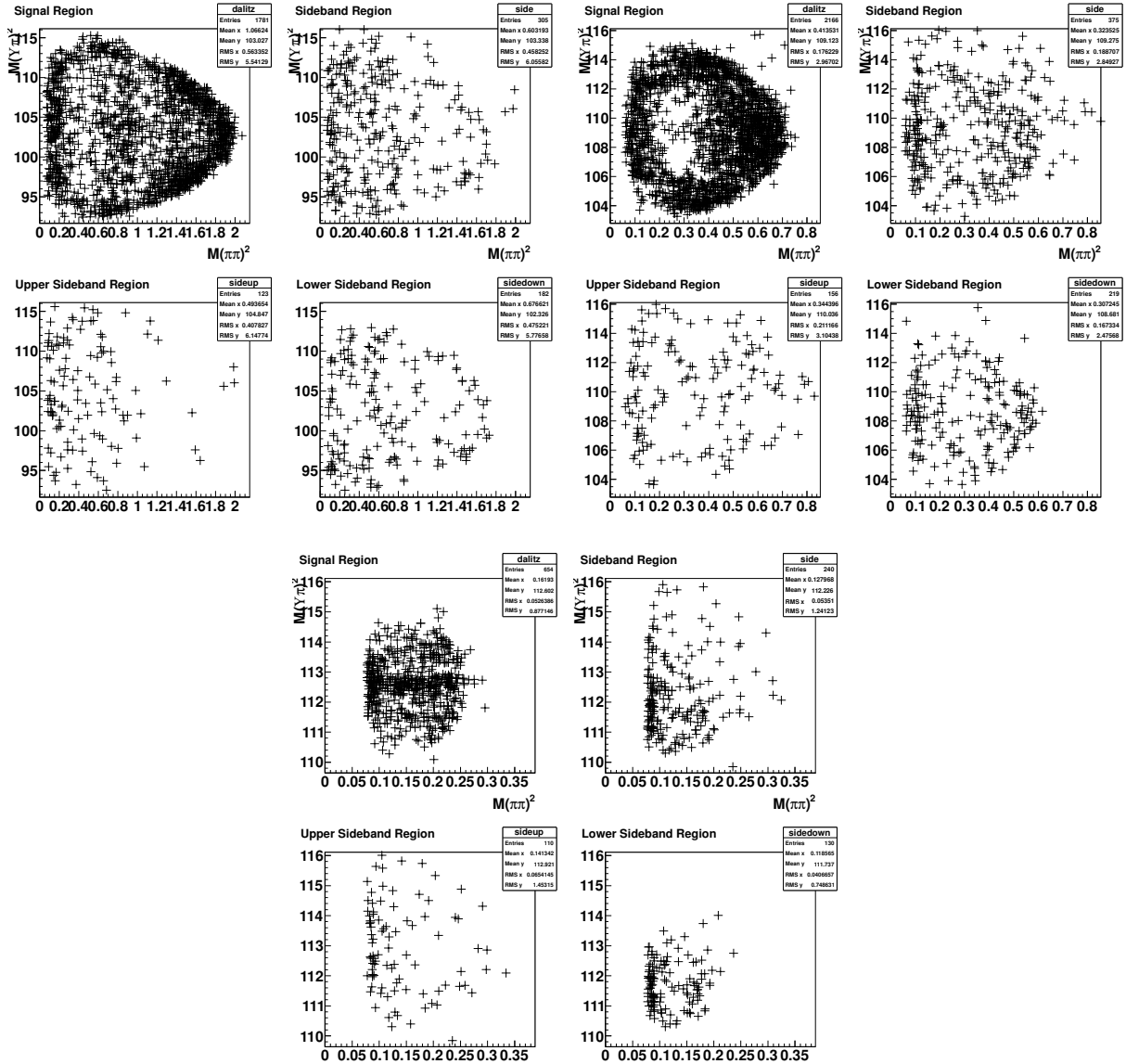
Figure E.4: Dalitz plots for 120 fb^{-1} of $\Upsilon(5S) \to \Upsilon(nS)\pi^+\pi^-$ data with both the v0finder and vertex separation cuts. Shown are the signal region (top left), total sidebands (top right), "upper" sideband (bottom left) and "lower" sideband (bottom right) for $\Upsilon(1S)$ (first block of four), $\Upsilon(2S)$ (second block of four), and $\Upsilon(3S)$ (third block of four).
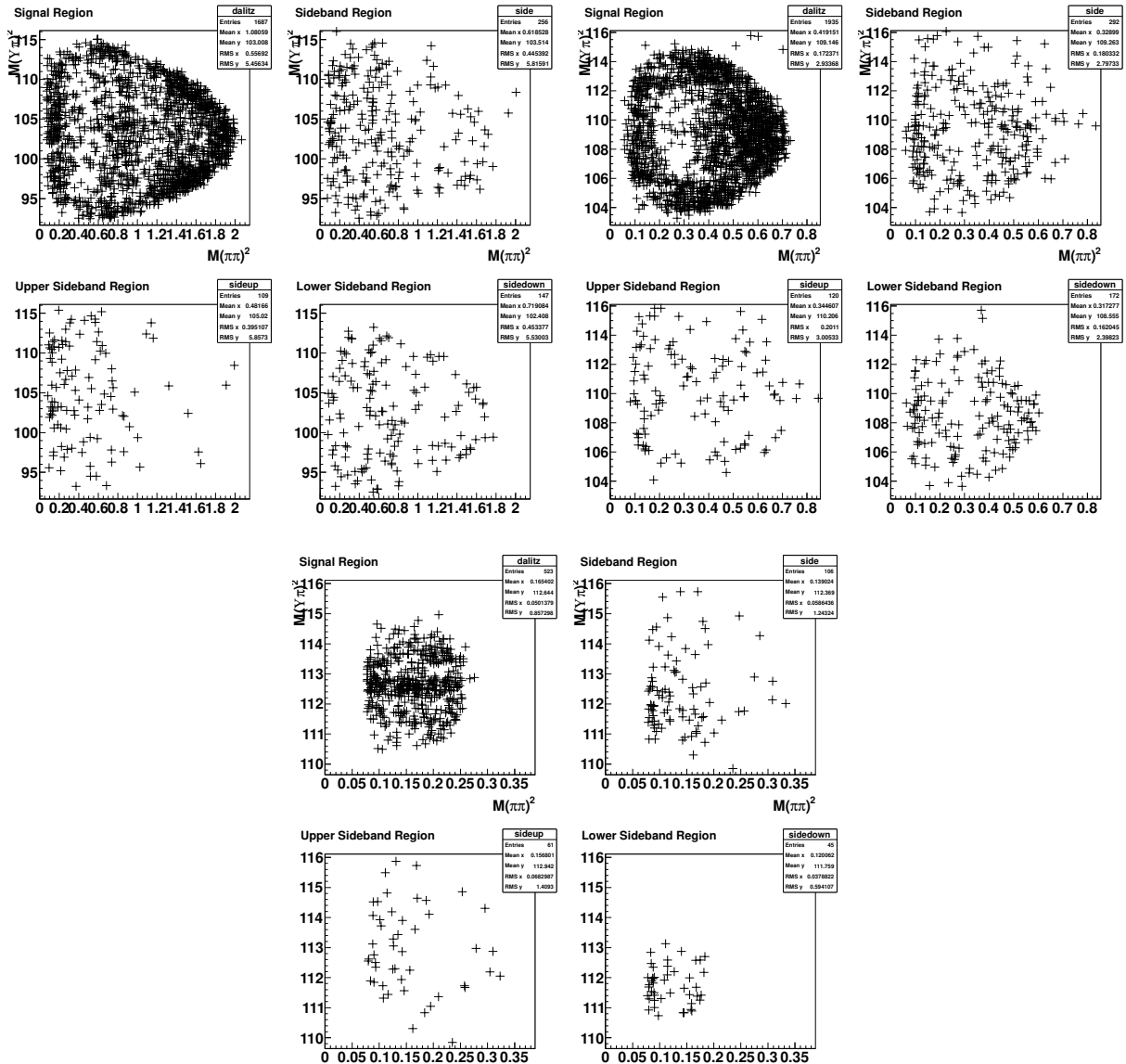
Figure E.5: Data sideband (black) and ISR MC (red) projections in $M_{\pi\pi}$ after the v0finder cut and before (left) and after (right) the vertex separation cuts for $\Upsilon(1S, 2S, 3S)$ modes.
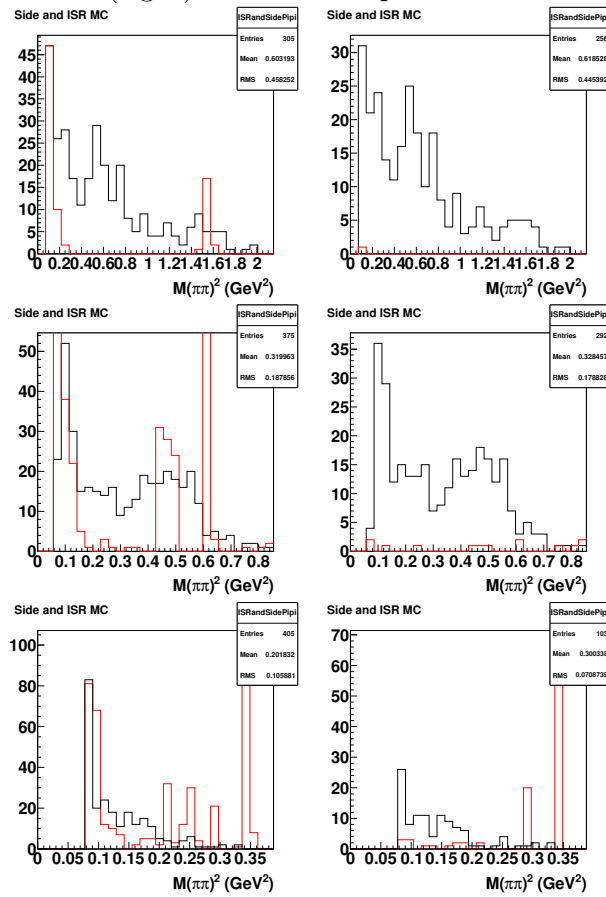
Figure E.6: Data sideband (black) and ISR MC (red, not to scale with estimated signal/background in data) projections in $M_{\pi\pi}$ before (left) and after (right) the v0finder ISR reduction for $\Upsilon(1S, 2S, 3S)$ modes.
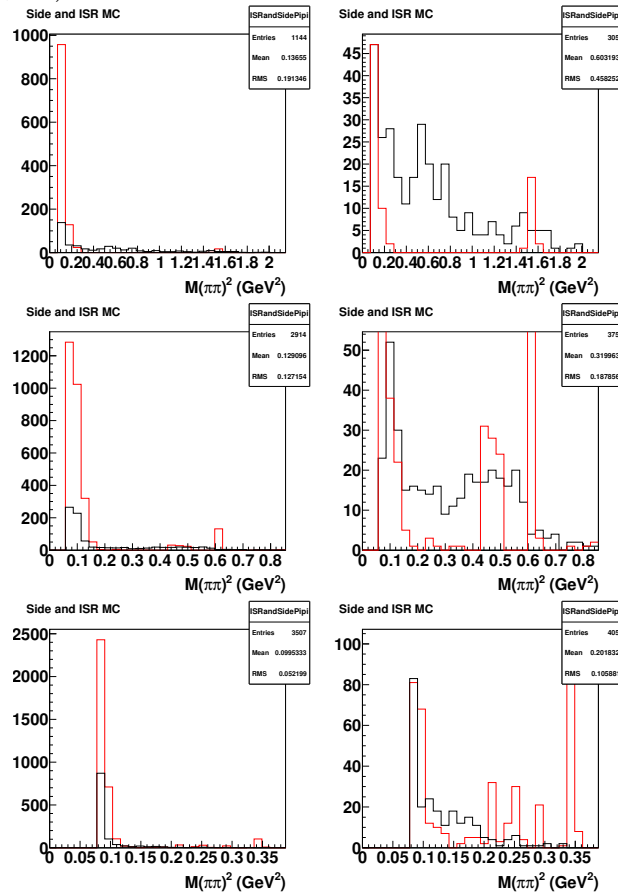
Figure E.7: Figure of merit ($signal/\sqrt{bg}$, top), signal efficiency (center), and number of photon conversion MC events not rejected for for the vertex separation cut, for $M_{\pi\pi}^2 < 140$ MeV^2 for $\Upsilon(2S)$.
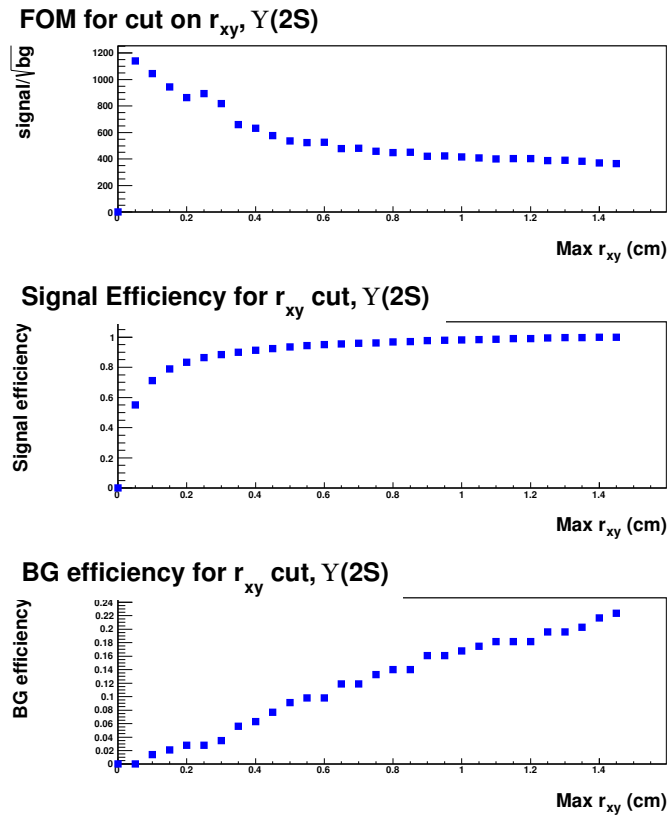
Figure E.8: Figure of merit ($signal/\sqrt{bg}$, top), signal efficiency (center), and number of photon conversion MC events not rejected for for the vertex separation cut, for $M_{\pi\pi}^2 < 100$ MeV^2 for $\Upsilon(3S)$.
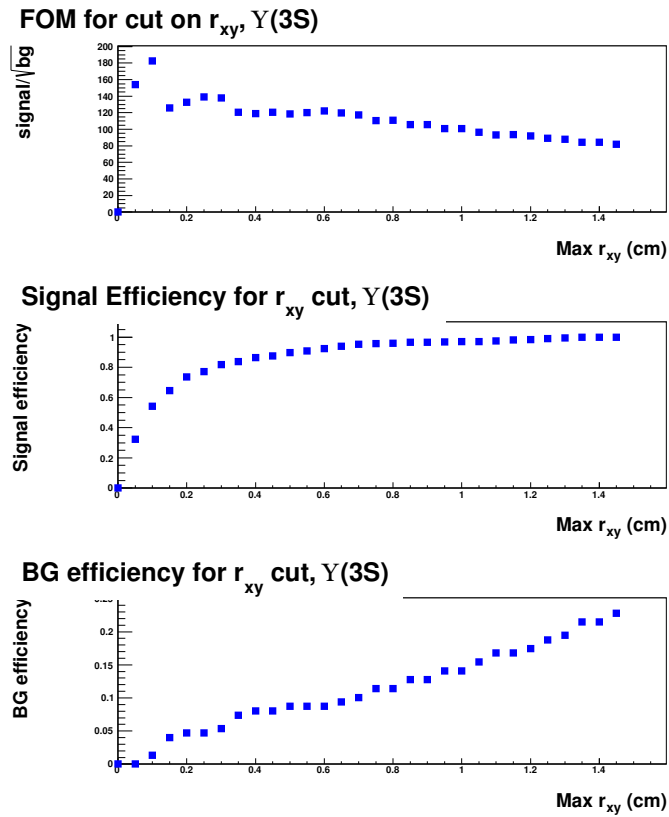
Appendix F

Ensembles of efficiency correction tests

Table F.1: Ensemble tests of efficiency correction, $\Upsilon(5S) \rightarrow \Upsilon(1S)\pi\pi$.

	Decay Process A	Process B	Process C	Process D
Num Experiments	100	100	100	50
Generated events/ea	100	100	100	1000
Gen Frac Z(10610)	.5	.25	.125	0
Gen Frac Z(10660)	.5	.25	.125	0
Gen Frac f0(980)	0	.25	.25	0
Gen Frac f2(1270)	0	.25	.25	0
Gen Frac PHSP	0	0	.25	1.0
Bias at 106	2.23	4.79	3.74	-0.41
RMS at 106	19.5	18.7	16.4	3.01
Bias at 107	13.9	7.08	2.49	0.321
RMS at 107	16.6	14.8	10.8	3.06
Bias at 108	11.1	4.38	1.91	1.49
RMS at 108	14.5	11.8	11.4	2.61
Bias at 11	7.34	3.65	1.42	-0.693
RMS at 11	11.1	10.5	11	3.12

Table F.2: Ensemble tests of efficiency correction, $\Upsilon(5S) \to \Upsilon(2S)\pi\pi$

	Decay Process A	Process B	Process C	Process D
Num Experiments	100	100	100	50
Generated events/ea	100	100	100	1000
Gen Frac Z(10610)	.5	.25	.125	0
Gen Frac Z(10660)	.5	.25	.125	0
Gen Frac f0(980)	0	.25	.25	0
Gen Frac f2(1270)	0	.25	.25	0
Gen Frac PHSP	0	0	.25	1.0
Bias at 106	-3.32	-0.18	-3.77	-1.31
RMS at 106	18.7	17.8	18.2	4.6
Bias at 107	9.65	5.91	5.8	2.7
RMS at 107	15.7	16.5	13.4	5.01
Bias at 108	12.3	10.7	6.14	1.97
RMS at 108	14.4	12.4	13.5	4.4
Bias at 11	11.1	7.73	4.24	-0.92
RMS at 11	12.9	10.8	10.6	4.03

Table F.3: Ensemble tests of efficiency correction, $\Upsilon(5S) \to \Upsilon(3S)\pi\pi$

	Decay Process A	Process B	Process C	Process D
Num Experiments	100	100	100	50
Generated events/ea	100	100	100	1000
Gen Frac Z(10610)	.5	.25	.125	0
Gen Frac Z(10660)	.5	.25	.125	0
Gen Frac f0(980)	0	.25	.25	0
Gen Frac f2(1270)	0	.25	.25	0
Gen Frac PHSP	0	0	.25	1.0
Bias at 106	0	0	0	0
RMS at 106	0	0	0	0
Bias at 107	-21.9	-22.8	-24.3	-41.5
RMS at 107	13.4	18.6	14.8	4.26
Bias at 108	4.67	1.98	1.77	-8.01
RMS at 108	15.9	16.9	16.1	5.25
Bias at 11	6.35	1.28	1.1	3.55
RMS at 11	14.4	15.5	13.3	4.37

Appendix G

Reproduction of the R_b fit, test of fitter

To ensure internal consistency, we attempt to reproduce the results of the R_b fit described in Belle Note 1214 [27]. We use the reported values and uncertainties for $\sqrt{s}$ and $\sigma_{b\bar{b}}/\sigma_{\mu\mu}$ and the same PDF,

$$\sigma = |A_{NR}|^2 + |A_R + A_{5S}e^{i\phi_{5S}}BW(M_{5S},\Gamma_{5S}) + A_{6S}e^{i\phi_{6S}}BW(M_{6S},\Gamma_{6S})|^2. \tag{G.1}$$

The results of a χ^2 fit to the data are compared to the results provided in BN1214v9 in Table G.1. The fit to the data is shown in Figure G.1. The fit results are consistent.

Table G.1: Fits to the R_b data from this analysis (top) and as reported in BN1214 [27] (bottom).

Fittype	χ^2/ndf	$\Upsilon(5S)$ M (GeV)	$\Upsilon(5S)$ σ (GeV)	$\Upsilon(5S)$ Amp	$\Upsilon(5S)$ ϕ Rad	$\Upsilon(6S)$ M (GeV)	$\Upsilon(6S)$ σ (GeV)	$\Upsilon(6S)$ Amp	$\Upsilon(6S)$ ϕ Rad	NonInt NR	Int NR
BN1307	70.8224/54	10.880241 ± 0.000977	0.051 ± 0.002	0.23	2.26 ± 0.05	11.00371 ± 0.00103	0.040 ± 0.002	0.20	-1.65 ± 0.10	0.40 ± 0.01	0.42 ± 0.00
BN1214	N/A	10.880400 ± 0.000900	0.051 ± 0.002	0.23	2.26 ± 0.05	11.00400 ± 0.00100	0.040 ± 0.002	0.20	-1.65 ± 0.07	0.38 ± 0.01	0.42 ± 0.01

Figure G.1: Fit of Equation G.1 to the R_b data reported in Reference [27].
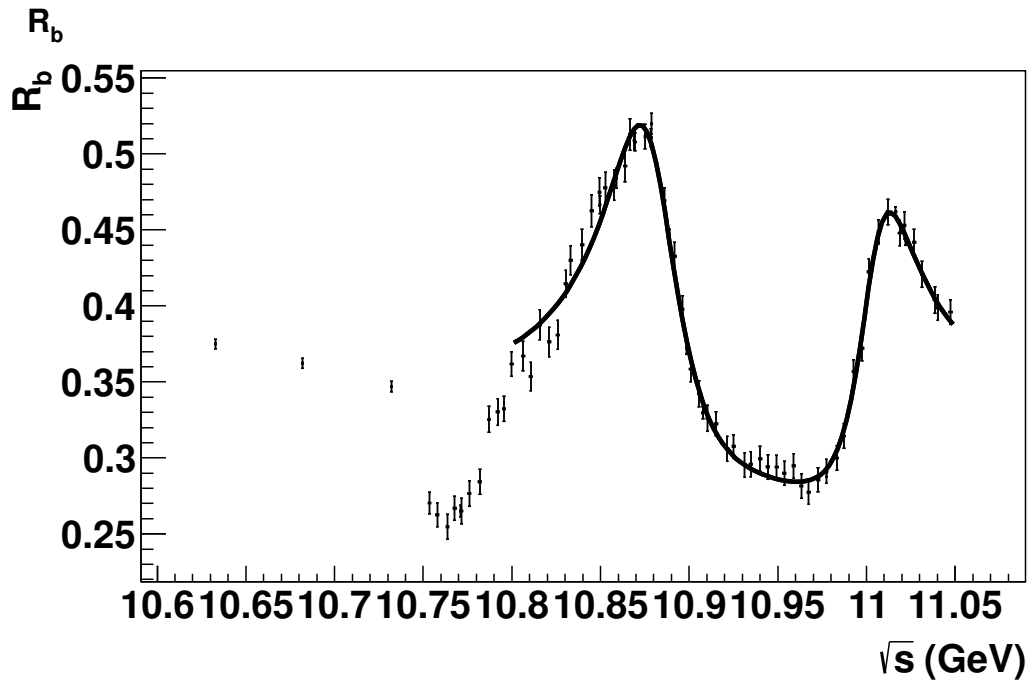
Bibliography

[1] *Phys. Rev. D*, 78:072004, 2008.

[2] *Phys. Rev. B*, 716:30, 2012.

[3] *Phys. Rev. B*, 716:1–29, 2012.

[4] A. Abashian et al. The belle detector. *Nuclear Instruments and Methods in Physics Research A*, 479:117–232, 2002.

[5] Ahmed Ali, Christian Hambrock, and M. Jamil Aslam. Tetraquark interpretation of the belle data on the anomalous $\upsilon(1s)\pi^+\pi^-$ and $\upsilon(2s)\pi^+\pi^-$ production near the $\upsilon(5s)$ resonance. *Phys. Rev. Lett.*, 104:162001, Apr 2010.

[6] B. Aubert, R. Barate, and others. Observation of a broad structure in the $\pi^+\pi^- j/\psi$ mass spectrum around 4.26 GeV/c^2. *Phys. Rev. Lett.*, 95:142001, Sep 2005.

[7] B. Aubert, M. Bona, Y. Karyotakis, and J. P. Lees. Measurement of the $e^+e^- \to b\bar{b}$ cross section between $\sqrt{s} = 10.54$ and 11.20 gev. *Phys. Rev. Lett.*, 102:012001, Jan 2009.

[8] A. Bondar, A. Garmash, R. Mizuk, D. Santel, K. Kinoshita, et al. Observation of two charged bottomoniumlike resonances in $\upsilon(5s)$ decays. *Phys. Rev. Lett.*, 108:122001, Mar 2012.

[9] R. Brun et al. Geant 3.21: The detector response simulator. *CERN Report*, DD/EE/84-1, 1984.

[10] K. F. Chen et al. *Phys. Rev. D*, 82:091106(R), 2010.

[11] K.-F. Chen, W.-S. Hou, M. Shapkin, A. Sokolov, et al. Observation of anomalous $\upsilon(1s)\pi^+\pi^-$ and $\upsilon(2s)\pi^+\pi^-$ production near the $\upsilon(5s)$ resonance. *Phys. Rev. Lett.*, 100:112001, Mar 2008.

[12] K.F. Chen et al. 2008.

[13] S.-K. Choi, S. L. Olsen, et al. Observation of a resonancelike structure in the $\pi\psi'$ mass distribution in exclusive $b \to k\pi\psi'$ decays. *Phys. Rev. Lett.*, 100:142001, Apr 2008.

[14] A. Garmash, A. Bondar, et al. *Unpublished Belle Note*, 2013.

[15] David Griffiths. *Introduction to Elementary Particles*. Wiley-VCH, 2nd edition, October 2008.

[16] H. Hirano et al. A high resolution cylindrical drift chamber for the kek b-factory. *Nuclear Instruments and Methods in Physics Research A*, 455:294, 2000.

[17] T. Iijima et al. Aerogel cherenkov counter for the belle detector. *Nuclear Instruments and Methods in Physics Research A*, 453:321, 2000.

[18] A. Kibayashi et al. The belle silicon vertex detector: Present performance and upgrade plan. *Nuclear Instruments and Methods in Physics Research A*, 501:22, 2003.

[19] H. Kichimi et al. The belle tof system. *Nuclear Instruments and Methods in Physics Research A*, 453:315, 2000.

[20] D. J. Lange et al. Evtgen generator. *Nuclear Instruments and Methods in Physics Research A*, 462:152, 2001.

[21] MissMJ. *Standard Model of Elementary Particles*. 2006.

[22] K. Miyabayashi et al. Belle electromagnetic calorimeter. *Nuclear Instruments and Methods in Physics Research A*, 494:298, 2002.

[23] Nakamura et al. *J. Phys. G*, 37:075021, 2010.

[24] Michael E. Peskin and Dan V. Schroeder. *An Introduction To Quantum Field Theory (Frontiers in Physics)*. Westview Press, October 1995.

[25] A. Ryd, D. Lange, N. Kuznetsova, et al. Evtgen user manual. *BAD*, 522 V6, 2004.

[26] N. A. Tornqvist. *Phys. Rev. Lett.*, 53:878880, 1984.

[27] Yuan-Pao Yang et al. *Unpublished Belle Note*, 1214 v9, 2012.

[28] Jure Zupan. Private Communication, 2013.